Monthly Notices of the ROYAL ASTRONOMICAL SOCIETY

MNRAS **443,** 3134–3156 (2014) doi:10.1093/mnras/stu1352

Neutrino-driven winds from neutron star merger remnants

A. Perego,[1,2★] S. Rosswog,[3] R. M. Cabezón,[2] O. Korobkin,[3] R. Käppeli,[4] A. Arcones[1] and M. Liebendörfer[2]

[1]*Institut für Kernphysik, Technische Universität Darmstadt, Schlossgartenstraße 2, D-64289 Darmstadt, Germany*
[2]*Physics Department, University of Basel, Klingelbergstrasse 82, CH-4056 Basel, Switzerland*
[3]*The Oskar Klein Centre, Department of Astronomy, Stockholm University, AlbaNova, SE-106 91 Stockholm, Sweden*
[4]*Seminar for Applied Mathematics, ETH Zürich, Rämistrasse 101, CH-8092 Zürich, Switzerland*

Accepted 2014 July 2. Received 2014 July 2; in original form 2014 May 26

ABSTRACT

We present a detailed, three-dimensional hydrodynamic study of the neutrino-driven winds emerging from the remnant of a neutron star merger. Our simulations are performed with the Newtonian, Eulerian code FISH, augmented by a detailed, spectral neutrino leakage scheme that accounts for neutrino absorption. Consistent with earlier two-dimensional studies, a strong baryonic wind is blown out along the original binary rotation axis within ≈100 ms. From this model, we compute a lower limit on the expelled mass of 3.5×10^{-3} $M_\odot$, relevant for heavy element nucleosynthesis. Because of stronger neutrino irradiation, the polar regions show substantially larger electron fractions than those at lower latitudes. The polar ejecta produce interesting r-process contributions from $A \approx 80$ to about 130, while the more neutron-rich, lower latitude parts produce elements up to the third r-process peak near $A \approx 195$. We calculate the properties of electromagnetic transients powered by the radioactivity in the wind, in addition to the 'macronova' transient stemming from the dynamic ejecta. The polar regions produce ultraviolet/optical transients reaching luminosities up to 10^{41} erg s^{-1}, which peak around 1 d in optical and 0.3 d in bolometric luminosity. The lower latitude regions, due to their contamination with high-opacity heavy elements, produce dimmer and more red signals, peaking after ∼2 d in optical and infrared.

Key words: accretion, accretion discs – dense matter – hydrodynamics – neutrinos – stars: neutron.

1 INTRODUCTION

Neutron star mergers play a key role for several branches of modern astrophysics. They are – together with neutron star–black hole coalescences – the major astrophysical target of the ground-based gravitational wave detector facilities such as LIGO, VIRGO and KAGRA (Acernese et al. 2008; Abbott et al. 2009; Harry & LIGO Scientific Collaboration 2010; Somiya 2012). Moreover, such compact binary mergers have been among the very early suggestions for the central engines of short gamma-ray bursts (sGRBs; Goodman 1986; Paczynski 1986; Eichler et al. 1989; Narayan, Paczynski & Piran 1992). While long GRBs (durations >2 s) very likely have a different origin, compact binary mergers are the most widely accepted engine for the category of short bursts (sGRBs). Over the years, however, contending models have emerged and the confrontation of the properties expected from compact binary mergers with those observed in sGRBs is not completely free of tension (see Piran 2004; Lee & Ramirez-Ruiz 2007; Nakar 2007; Gehrels, Ramirez-Ruiz & Fox 2009; Berger 2011, 2013, for recent reviews). A binary neutron star merger (hereafter BNS merger) forms initially a central, hypermassive neutron star (HMNS) surrounded by a thick accretion disc. During the merger process a small fraction of the total mass becomes ejected via gravitational torques and hydrodynamic processes ('dynamic ejecta'). The decompression of this initially cold and extremely neutron-rich nuclear matter had long been suspected to provide favourable conditions for the formation of heavy elements through the rapid neutron capture process (the 'r-process'; Lattimer & Schramm 1974; Lattimer & Schramm 1976; Lattimer et al. 1977; Symbalisty & Schramm 1982; Eichler et al. 1989; Meyer 1989; Davies et al. 1994). While initially only considered as an 'exotic' or second-best model behind core-collapse supernovae, there is nowadays a large literature that – based on hydrodynamical and nucleosynthetic calculations – consistently finds that the dynamic ejecta of a neutron star merger is an extremely promising site for the formation of the heaviest elements with $A > 130$ (see e.g. Freiburghaus, Rosswog & Thielemann 1999; Rosswog et al. 1999; Oechslin, Janka & Marek 2007; Metzger et al. 2010b; Goriely, Bauswein & Janka 2011a; Goriely et al. 2011b; Roberts et al. 2011; Korobkin et al. 2012; Bauswein, Goriely

★ E-mail: albino.perego@physik.tu-darmstadt.de

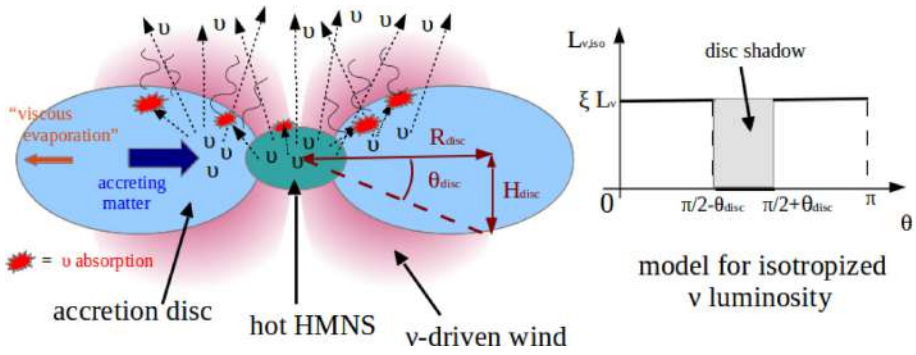

Figure 1. Left: sketch of the neutrino-driven wind from the remnant of a BNS merger. The hot HMNS and the accretion disc emit neutrinos, preferentially along the polar direction and at intermediate latitudes. A fraction of the neutrinos is absorbed by the disc and can lift matter out of its gravitational potential. On the viscous time-scale, matter is also ejected along the equatorial direction. Right: sketch of the isotropized ν luminosity we are using for our analytical estimates (see the main text for details).

& Janka 2013; Hotokezaka et al. 2013; Kyutoku, Ioka & Shibata 2013; Wanajo et al. 2014). Core-collapse supernovae, on the contrary, seem seriously challenged in generating the conditions that are needed to produce elements with $A > 90$ (Arcones, Janka & Scheck 2007; Fischer et al. 2010; Hüdepohl et al. 2010; Roberts, Woosley & Hoffman 2010). A possible exception, though, may be magnetically driven explosions of rapidly rotating stars (Winteler et al. 2012; Mösta et al. 2014). Such explosions, however, require a combination of rather extreme properties of the pre-explosion star and are therefore likely rare.

Most recently, the idea that compact binary mergers are related to both sGRBs and the nucleosynthesis of the heaviest elements has gained substantial observational support. In 2013 June, the *Swift* satellite detected a relatively nearby ($z = 0.356$) sGRB, GRB 130603B (Melandri et al. 2013), for which the *Hubble Space Telescope* (Berger, Fong & Chornock 2013a; Tanvir et al. 2013) detected a near-infrared (NIR) point source, 9 d after the burst. The properties of this second detection are close to model predictions (Barnes & Kasen 2013; Kasen, Badnell & Barnes 2013; Tanaka & Hotokezaka 2013; Grossman et al. 2014; Rosswog et al. 2014a; Tanaka et al. 2014) for the so-called 'macro-' or 'kilonovae' (Li & Paczyński 1998; Kulkarni 2005; Rosswog 2005; Metzger et al. 2010a,b; Roberts et al. 2011), radioactively powered transients from the decay of freshly produced r-process elements. In particular, the delay of several days between the sGRB and the NIR detection is consistent with the expanding material having very large opacities, as predicted for very heavy r-process elements (Kasen et al. 2013). If this interpretation is correct, GRB 130603B would provide the first observational confirmation of the long-suspected link between compact binary mergers, heavy elements nucleosynthesis and GRBs.

There are at least two more channels, apart from the dynamic ejecta, by which a compact binary merger releases matter into space, and both of them are potentially interesting for nucleosynthesis and – if enough long-lived radioactive material is produced – they may also power additional electromagnetic transients. The first channel is the post-merger accretion disc. As it evolves viscously, expands and cools, the initially completely dissociated matter recombines into α-particles and – together with viscous heating – releases enough energy to unbind an amount of material that is comparable to the dynamic ejecta (Beloborodov 2008; Metzger, Piro & Quataert 2008, 2009; Lee, Ramirez-Ruiz & López-Cámara 2009; Fernández & Metzger 2013).

The second additional channel is related to neutrino-driven winds, the basic mechanisms of which are sketched in Fig. 1. This wind is, in several respects, similar to the one that emerges from protoneutron stars. In particular, in both cases a similar amount of gravitational binding energy is released over a comparable (neutrino diffusion) time-scale, which results in a luminosity of $L_\nu \sim \Delta E_{\rm grav}/\tau_{\rm diff} \sim 10^{53}$ erg s^{-1} and neutrinos with energies ∼10–15 MeV. Under these conditions, energy deposition due to neutrino absorption is likely to unbind a fraction of the merger remnant. In contrast to protoneutron stars, however, the starting point is extremely neutron-rich nuclear matter, rather than a deleptonizing stellar core. At remnant temperatures of several MeV, electron antineutrinos dominate over electron neutrinos, contrary to the protoneutron star case. Based on scaling relations from the protoneutron star context (Duncan, Shapiro & Wasserman 1986; Qian & Woosley 1996), early investigations discussed neutrino-driven winds from merger remnants either in an order-of-magnitude sense or via parametrized models (Ruffert et al. 1997; Rosswog & Ramirez-Ruiz 2002; Rosswog & Liebendörfer 2003; McLaughlin & Surman 2005; Surman, McLaughlin & Hix 2006; Metzger et al. 2008; Surman et al. 2008; Caballero, McLaughlin & Surman 2012; Wanajo & Janka 2012). To date, only one neutrino hydrodynamics calculation for merger remnants has been published (Dessart et al. 2009). This study was performed in two dimensions with the code VULCAN/two-dimensional (2D) and drew its initial conditions from three-dimensional (3D) smoothed particle hydrodynamics (SPH) calculations with similar input physics, but without modelling the heating due to neutrinos (Price & Rosswog 2006). These calculations confirmed indeed that a neutrino-driven wind develops (with $\dot{M} \sim 10^{-3}$ M$_\odot$ s^{-1}), blown out into the funnel along the binary rotation axis that was previously thought to be practically baryon free. By baryon loading the suspected launch path, this wind could potentially threaten the emergence of the ultrarelativistic outflow that is needed for a short GRB. Dessart et al. (2009) therefore concluded that the launch of a sGRB was unlikely to happen in the presence of the HMNS, but could possibly occur after the collapse to a black hole. The implications of a baryon loaded wind for the expansion of a relativistic jet in successful sGRB production have been recently investigated by Murguia-Berthier et al. (2014). They found that, for relatively long collapse time-scales of the HMNS ($\gtrsim$100 ms), a jet will likely not be able to break out from the wind during the typical duration of a sGRB.

The aim of this study is to explore further neutrino-driven winds from compact binary mergers remnants. We focus here on the phase

where a HMNS is present in the centre and we assume that it does not collapse during the time frame of our simulation, as in Dessart et al. (2009). Given the various stabilizing mechanism such as thermal support, possibly magnetic fields and in particular the strong differential rotation of the HMNS together with a lower limit on the maximum mass in excess of 2.0 $M_\odot$ (Demorest et al. 2010; Antoniadis et al. 2013), we consider this as a very plausible assumption. We are mainly interested to see how robust the previous 2D results are with respect to a transition to three spatial dimensions. The questions about the understanding of the heavy element nucleosynthesis that occurs in compact binary mergers, the prediction of observable electromagnetic counterparts for the different outflows, and the emergence of sGRBs are the main drivers behind this work.

This paper is organized as follows. In Section 2, we estimate the most important disc and wind time-scales. The details of our numerical model are explained in Section 3. In addition, we briefly present the merger simulation, the outcome of which is used as initial condition for our study. Our results are presented in Section 4. We briefly discuss in Section 5 the nucleosynthesis in the neutrino-driven wind and the properties of the radioactively powered, electromagnetic transients that result from them. Our major results are finally summarized in Section 6.

2 ANALYTICAL ESTIMATES

The properties of the remnant of a BNS merger can vary significantly (see e.g. Bauswein et al. 2013; Hotokezaka et al. 2013; Rosswog, Piran & Nakar 2013; Wanajo et al. 2014, and references therein), depending on the binary parameters (mass, mass ratio, eccentricity, spins, etc.) and on the nuclear equation of state (hereafter EoS). For our estimates and scaling relations, we use numerical values that characterize our initial model, see Section 3.3 for more details.

We consider a central HMNS of mass $M_{\rm ns} \approx 2.5\,{\rm M}_\odot$, radius $R_{\rm ns} \approx 25\,{\rm km}$ and temperature $k_{\rm B}T_{\rm ns} \approx 15\,{\rm MeV}$. Inside of it, neutrinos are assumed to be in thermal equilibrium with matter. Under these conditions the typical neutrino energy can be estimated as $E_{\nu,{\rm ns}} \sim (F_3(0)/F_2(0))\,k_{\rm B}T_{\rm ns} \approx 3.15\,k_{\rm B}T_{\rm ns} \approx 50\,{\rm MeV}$, where $F_n(0)$ is the Fermi integral of order n, evaluated for a vanishing degeneracy parameter. The central object is surrounded by a geometrically thick disc of mass $M_{\rm disc} \approx 0.2\,{\rm M}_\odot$, radius $R_{\rm disc} \approx 100\,{\rm km}$ and height $H_{\rm disc} \approx 33\,{\rm km}$. The aspect ratio of the disc is then $H/R \approx 1/3$. We assume a neutrino energy in the disc of $E_{\nu,\,{\rm disc}} \sim 15\,{\rm MeV}$, comparable with the mean energy of the ultimately emitted neutrinos (see e.g. Rosswog et al. 2013).

Representative density values in the HMNS and in the disc are $\rho_{\rm ns} \sim 10^{14}\,{\rm g\,cm^{-3}}$ and $\rho_{\rm disc} \sim 5 \times 10^{11}\,{\rm g\,cm^{-3}}$, respectively.

The *dynamical time-scale* $t_{\rm dyn}$ of the disc is set by the orbital Keplerian motion around the HMNS:

$$t_{\rm dyn} \sim \frac{2\pi}{\Omega_{\rm K}} \approx 0.011\,{\rm s}\left(\frac{M_{\rm ns}}{2.5\,{\rm M}_\odot}\right)^{-1/2}\left(\frac{R_{\rm disc}}{100\,{\rm km}}\right)^{3/2}, \quad (1)$$

where $\Omega_{\rm K}$ is the Keplerian angular velocity.

On a time-scale longer than $t_{\rm dyn}$, viscosity drives radial motion. Assuming it can be described by an α-parameter model (Shakura & Sunyaev 1973), we estimate the *lifetime of the accretion disc* $t_{\rm disc}$ as

$$t_{\rm disc} \sim \alpha^{-1}\left(\frac{H}{R}\right)^{-2}\Omega_{\rm K}^{-1} \approx 0.3\,{\rm s}\left(\frac{\alpha}{0.05}\right)^{-1}\left(\frac{H/R}{1/3}\right)^{-2} \times \left(\frac{M_{\rm ns}}{2.5\,{\rm M}_\odot}\right)^{-1/2}\left(\frac{R_{\rm disc}}{100\,{\rm km}}\right)^{3/2}. \quad (2)$$

The *accretion rate* on the HMNS $\dot{M}$ is then of order

$$\dot{M} \sim \frac{M_{\rm disc}}{t_{\rm disc}} \approx 0.64\,\frac{{\rm M}_\odot}{\rm s}\left(\frac{M_{\rm disc}}{0.2\,{\rm M}_\odot}\right)\left(\frac{\alpha}{0.05}\right) \times \left(\frac{H/R}{1/3}\right)^2\left(\frac{M_{\rm ns}}{2.5\,{\rm M}_\odot}\right)^{1/2}\left(\frac{R_{\rm disc}}{100\,{\rm km}}\right)^{-3/2}. \quad (3)$$

Neutrinos are the major cooling agent of the remnant. Neutrino scattering off nucleons is one of the major sources of *opacity* for all neutrino species[1] and the corresponding mean free path can be estimated as

$$\lambda_{N\nu} \approx 7.44 \times 10^3\,{\rm cm}\left(\frac{\rho}{10^{14}\,{\rm g\,cm^{-3}}}\right)^{-1}\left(\frac{E_\nu}{10\,{\rm MeV}}\right)^{-2}, \quad (4)$$

where ρ is the matter density and E_ν is the typical neutrino energy. The large variation in density between the HMNS and the disc suggests to treat these two regions separately.

For the central compact object, the *cooling time-scale* $t_{\rm cool,\,ns}$ is governed by neutrino diffusion (see e.g. Rosswog & Liebendörfer 2003). If $\tau_{\nu,\,{\rm ns}}$ is the neutrino *optical depth* inside the HMNS, then

$$t_{\rm cool,ns} \sim 3\,\frac{\tau_{\nu,{\rm ns}}\,R_{\rm ns}}{c}. \quad (5)$$

If we assume $\tau_{\nu,\,{\rm ns}} \sim R_{\rm ns}/\lambda_{N\nu}$,

$$t_{\rm cool,ns} \sim 1.88\,{\rm s}\left(\frac{R_{\rm ns}}{25\,{\rm km}}\right)^2\left(\frac{\rho_{\rm ns}}{10^{14}\,{\rm g\,cm^{-3}}}\right)\left(\frac{k_{\rm B}T_{\rm ns}}{15\,{\rm MeV}}\right)^2. \quad (6)$$

The neutrino luminosity coming from the HMNS is powered by an internal energy reservoir $\Delta E_{\rm ns}$. We estimate it as the difference between the internal energy of a hot and of a cold HMNS. For the first one, we consider typical profiles of a HMNS obtained from a BNS merger simulation. For the second one, we set $T = 0$ everywhere inside it. Under these assumptions, $\Delta E_{\rm ns} \approx 0.30\,E_{\rm int,\,HMNS} \approx 3.4 \times 10^{52}\,{\rm erg}$, and the associated HMNS neutrino luminosity (integrated over all neutrino species) is approximately

$$L_{\nu,{\rm ns}} \sim \frac{\Delta E_{\rm ns}}{t_{\rm diff,ns}} \approx 1.86 \times 10^{52}\,\frac{\rm erg}{\rm s}\left(\frac{\Delta E_{\rm ns}}{3.5 \times 10^{52}\,{\rm erg}}\right) \times \left(\frac{R_{\rm ns}}{25\,{\rm km}}\right)^{-2}\left(\frac{\rho_{\rm ns}}{10^{14}\,{\rm g\,cm^{-3}}}\right)^{-1}\left(\frac{k_{\rm B}T_{\rm ns}}{15\,{\rm MeV}}\right)^{-2}. \quad (7)$$

The disc diffusion time-scale can be estimated using an analogous to equation (5):

$$t_{\rm cool,disc} \sim 3\,\frac{\tau_{\nu,{\rm disc}}\,H_{\rm disc}}{c} \approx 1.68\,{\rm ms}\left(\frac{H_{\rm disc}}{33\,{\rm km}}\right)^2 \times \left(\frac{\rho_{\rm disc}}{5 \times 10^{11}\,{\rm g\,cm^{-3}}}\right)\left(\frac{E_{\nu,{\rm disc}}}{15\,{\rm MeV}}\right)^2. \quad (8)$$

Because of this fast cooling time-scale, a persistent neutrino luminosity from the disc requires a constant supply of internal energy. In an accretion disc, this is provided by the *accretion mechanism*: while matter falls into deeper Keplerian orbits, the released gravitational energy is partially (∼50 per cent) converted into internal energy. If $R_{\rm disc} \sim 100\,{\rm km}$ denotes the typical initial distance inside the disc, and the radius of the HMNS is assumed to be the final one, then $\Delta E_{\rm grav} \sim (GM_{\rm ns}M_{\rm disc}/R_{\rm ns})$, where we have used $R_{\rm ns}^{-1} \gg R_{\rm disc}^{-1}$.

[1] In the case of $\nu_{\rm e}$s, the opacity related with absorption by neutrons is even larger. Nevertheless, it is still comparable to the scattering off nucleons.

The neutrino luminosity for the accretion process is approximately

$$L_{\nu,\mathrm{disc}} \sim 0.5\,\frac{\Delta E_{\mathrm{grav}}}{t_{\mathrm{disc}}} \approx 8.35\times\ 10^{52}\,\frac{\mathrm{erg}}{\mathrm{s}}\left(\frac{M_{\mathrm{ns}}}{2.5\,\mathrm{M}_\odot}\right)^{3/2}\left(\frac{\alpha}{0.05}\right)$$
$$\times\left(\frac{M_{\mathrm{disc}}}{0.2\,\mathrm{M}_\odot}\right)\left(\frac{H/R}{1/3}\right)^{2}\left(\frac{R_{\mathrm{disc}}}{100\,\mathrm{km}}\right)^{-3/2}\left(\frac{R_{\mathrm{ns}}}{25\,\mathrm{km}}\right)^{-1}. \quad (9)$$

Note that during the disc accretion phase $L_{\nu,\,\mathrm{disc}}$ is larger than $L_{\nu,\,\mathrm{ns}}$. Together, the HMNS and the disc release neutrinos at a luminosity of $\sim 10^{53}$ erg s^{-1}, consistent with the simple estimate from the Introduction.

Because of the density (opacity) structure of the disc, the neutrino emission is expected to be anisotropic, with a larger luminosity in the polar directions ($\theta = 0$ and $\theta = \pi$), compared to the one along the equator ($\theta = \pi/2$), see also Rosswog, Ramirez-Ruiz & Davies (2003) and Dessart et al. (2009). For a simple model of this effect, we assume that the disc creates an axisymmetric shadow area across the equator, while the emission is uniform outside this area. The amplitude of the shadow is $2\,\theta_{\mathrm{disc}}$, where $\tan\theta_{\mathrm{disc}} = (H/R)$. Then, we define an isotropized axisymmetric luminosity $L_{\nu,\,\mathrm{iso}}(\theta)$ as (see the sketch on the right in Fig. 1)

$$L_{\nu,\mathrm{iso}}(\theta) = \begin{cases} \xi\,L_\nu & \text{for } |\theta - \pi/2| > \theta_{\mathrm{disc}}, \\ 0 & \text{for } |\theta - \pi/2| \le \theta_{\mathrm{disc}}. \end{cases} \quad (10)$$

The value of ξ is set by the normalization of $L_{\nu,\,\mathrm{iso}}$ over the whole solid angle Ω, $\int_\Omega L_{\nu,\,\mathrm{iso}}\,\mathrm{d}\Omega = L_\nu$:

$$\xi = \frac{1}{1-\sin\theta_{\mathrm{disc}}}. \quad (11)$$

For $(H/R) \approx 1/3$, one finds $\theta_{\mathrm{disc}} \approx \pi/10$ and $\xi \approx 1.5$.

After having determined approximate expressions for the neutrino luminosities, we are ready to estimate the relevant time-scale for the formation of the ν-driven wind.

We define the *wind time-scale* t_{wind} as the time necessary for the matter to absorb enough energy to overcome the gravitational well generated by the HMNS. This energy deposition happens inside the disc and it is due to the re-absorption of neutrinos emitted at their last interaction surface. Thus,

$$t_{\mathrm{wind}} \sim e_{\mathrm{grav}}/\dot{e}_{\mathrm{heat}}, \quad (12)$$

where $e_{\mathrm{grav}} \approx GM_{\mathrm{ns}}/R$ is the specific gravitational energy, and $\dot{e}_{\mathrm{heat}}$ is the specific heating rate provided by neutrino absorption at a radial distance R from the centre:

$$\dot{e}_{\mathrm{heat}} \sim k\,\frac{L_{\nu_{\mathrm{e}},\mathrm{iso}}(|\theta-\pi/2| > \theta_{\mathrm{disc}})}{4\pi\,R^2}. \quad (13)$$

In the equation above we have assumed that $L_{\nu_{\mathrm{e}}} \approx L_{\bar{\nu}_{\mathrm{e}}} \sim \left(L_{\nu,\mathrm{ns}} + L_{\nu,\mathrm{disc}}\right)/3$. If $k \approx 5.65\times\ 10^{-20}\,\mathrm{cm^2\,g^{-1}\,MeV^{-2}}$, E_ν^2 is the typical absorptivity on nucleons (Bruenn 1985), the heating rate can be re-expressed as

$$\dot{e}_{\mathrm{heat}} \sim 4.6\times\ 10^{20}\,\frac{\mathrm{erg}}{\mathrm{g\,s}}\left(\frac{R}{100\,\mathrm{km}}\right)^{-2}$$
$$\times\left(\frac{L_{\nu_{\mathrm{e}}}}{3\times\ 10^{52}\,\mathrm{erg\,s^{-1}}}\right)\left(\frac{\xi}{1.5}\right)\left(\frac{E_{\nu,\mathrm{disc}}}{15\,\mathrm{MeV}}\right)^{2}. \quad (14)$$

Finally, the wind time-scale, equation (12), becomes

$$t_{\mathrm{wind}} \sim 0.07\,\mathrm{s}\left(\frac{M_{\mathrm{ns}}}{2.5\,\mathrm{M}_\odot}\right)\left(\frac{R}{100\,\mathrm{km}}\right)$$
$$\times\left(\frac{L_{\nu_{\mathrm{e}}}}{3\times\ 10^{52}\,\mathrm{erg\,s^{-1}}}\right)^{-1}\left(\frac{\xi}{1.5}\right)^{-1}\left(\frac{E_{\nu,\mathrm{disc}}}{15\,\mathrm{MeV}}\right)^{-2}. \quad (15)$$

Since $t_{\mathrm{wind}} < t_{\mathrm{disc}}$, neutrino heating can drive a wind within the lifetime of the disc. Moreover, since the disc provides a substantial fraction of the total neutrino luminosity, a wind can form also in the absence of the HMNS.

Of course, the neutrino emission processes are much more complicated than what can be captured by these simple estimates. Nevertheless, they provide a reasonable first guidance for the qualitative understanding of the remnant evolution.

3 NUMERICAL MODEL FOR THE REMNANT EVOLUTION

3.1 Hydrodynamics

We perform our simulations with the FISH code (Käppeli et al. 2011). FISH is a parallel grid code that solves the equations of ideal, Newtonian hydrodynamics (HD):[2]

$$\frac{\partial\rho}{\partial t} + \nabla\cdot(\rho\boldsymbol{v}) = 0, \quad (16)$$

$$\frac{\partial\rho\boldsymbol{v}}{\partial t} + \nabla\cdot(\rho\boldsymbol{v}\otimes\boldsymbol{v}) + \nabla p = -\rho\nabla\phi + \rho\left(\frac{\mathrm{d}\boldsymbol{v}}{\mathrm{d}t}\right)_\nu, \quad (17)$$

$$\frac{\partial E}{\partial t} + \nabla\cdot[(E+p)\,\boldsymbol{v}] = -\rho\boldsymbol{v}\nabla\phi + \rho\left(\frac{\mathrm{d}e}{\mathrm{d}t}\right)_\nu, \quad (18)$$

$$\frac{\partial\rho Y_{\mathrm{e}}}{\partial t} + \nabla\cdot(\rho Y_{\mathrm{e}}\boldsymbol{v}) = \rho\left(\frac{\mathrm{d}Y_{\mathrm{e}}}{\mathrm{d}t}\right)_\nu. \quad (19)$$

Here ρ is the mass density, $\boldsymbol{v}$ the velocity, $E = \rho e + \rho v^2/2$ the total energy density (i.e. the sum of internal and kinetic energy density), e the specific internal energy, p the matter pressure and Y_{e} the electron fraction. The code solves the HD equations with a second-order accurate finite volume scheme on a uniform Cartesian grid. The source terms on the right-hand side stem from gravity and from neutrino–matter interactions. We notice that the viscosity of our code is of numerical nature, while no physical viscosity is explicitly included. The neutrino source terms will be discussed in detail in Section 3.2. The gravitational potential ϕ obeys the Poisson equation

$$\nabla^2\phi = 4\pi G\rho, \quad (20)$$

where G is the gravitational constant. The merger of two neutron stars with equal masses is expected to form a highly axisymmetric remnant. We exploit this approximate invariance by solving the Poisson equation in cylindrical symmetry. This approximation results in a high gain in computational efficiency, given the elliptic (and hence global) nature of equation (20). To this end, we *conservatively* average the 3D density distribution on to an axisymmetric grid, having the HMNS rotational axis as the symmetry axis. The Poisson equation is then solved with a fast multigrid algorithm (Press et al. 1992), and the resulting potential is interpolated back on the 3D grid.

The HD equations are closed by an EoS relating the internal energy to the pressure. In our model, we use the TM1 EoS description of nuclear matter supplemented with electron–positron and photon contributions, in tabulated form (Timmes & Swesty 2000; Hempel

[2] FISH can actually solve the equations of ideal magnetohydrodynamics. However, we have not included magnetic fields in our current set-up.

Table 1. List of the neutrino reactions included in the simulation (left-hand column; $\nu \equiv \nu_e, \bar{\nu}_e, \nu_{\mu,\tau}$), of their major effects (central column; O stands for opacity, P for neutrino production and T for neutrino thermalization), and of the references for the implementation (right-hand column): 'a' corresponds to Bruenn (1985), 'b' to Mezzacappa & Bruenn (1993) and 'c' to Hannestad & Raffelt (1998).

Reaction	Roles	Ref.
$e^- + p \leftrightarrow n + \nu_e$	O, T, P	a
$e^+ + n \leftrightarrow p + \bar{\nu}_e$	O, T, P	a
$e^- + (A, Z) \leftrightarrow \nu_e + (A, Z-1)$	T, P	a
$N + \nu \leftrightarrow N + \nu$	O	a
$(A, Z) + \nu \leftrightarrow (A, Z) + \nu$	O	a
$e^+ + e^- \leftrightarrow \nu + \bar{\nu}$	T, P	a, b
$N + N \leftrightarrow N + N + \nu + \bar{\nu}$	T, P	c

et al. 2012). This description is equivalent to one provided by the Shen et al. EoS (Shen et al. 1998a,b) in the high-density part.

3.2 Neutrino treatment

In general, the multidimensional neutrino transport is described by the equation of radiative transfer (see e.g. Mihalas & Mihalas 1984). Instead of a direct solution of this equation, which is computationally very expensive in large multidimensional simulations, we employ a relatively inexpensive, effective neutrino treatment. Our goal is to provide expressions for the neutrino source terms, assuming to know qualitatively the solution of the radiative transfer equation in different parts of the domain. Our treatment is a spectral extension of previous grey leakage schemes (Ruffert, Janka & Schaefer 1996; Rosswog & Liebendörfer 2003). However, differently from its predecessors, it includes also *spectral absorption terms in the optically thin regime*. We refer to it as an Advanced Spectral Leakage (ASL) scheme.[3] The treatment has been developed and tested against detailed Boltzmann neutrino transport for spherically symmetric core collapse supernova models. For two tested progenitors (15 and 40 $M_\odot$ zero-age main-sequence stars), the neutrino luminosities and the shock positions agree within 20 per cent with the corresponding values obtained by Boltzmann transport, for a few hundreds of milliseconds after core bounce. A detailed description with tests will be discussed in a separate paper (Perego et al., in preparation).

The ASL scheme models explicitly three different neutrino species: ν_e, $\bar{\nu}_e$ and $\nu_{\mu,\tau}$. The species $\nu_{\mu,\tau}$ is a collective species for μ and τ (anti)neutrinos that contributes only as a source of cooling in the energy equation. The neutrino energy is discretized in 12 geometrically increasing energy bins, chosen in the range $2 \leq E_\nu \leq 200$ MeV. The ASL scheme includes the reactions listed in Table 1. They correspond to the reactions that we expect to be more relevant in hot and dense matter. Neutrino pair annihilation is included only as a source of opacity in optically thick conditions. Because of the geometry of the emission, it is also supposed to be important in optically thin conditions (see e.g. Janka 1991; Burrows, Reddy & Thompson 2006). For the application to the BNS merger scenario, see Dessart et al. (2009) and references therein. Therefore, our numbers concerning the mass loss $\dot{M}$ need to be considered as lower limits on the true value. The full inclusion of this process in our model will be performed in a future step.

The neutrino optical depths τ_νs play a central role in our scheme. We distinguish between the *scattering* ($\tau_{\nu,\mathrm{sc}}$) and the *energy* ($\tau_{\nu,\mathrm{en}}$) spectral optical depth. The first one is obtained by summing all the relevant neutrino processes:

$$\mathrm{d}\tau_{\nu,\mathrm{sc}} = \rho\,(k_{\mathrm{sc}} + k_{\mathrm{ab}})\,\mathrm{d}s, \tag{21}$$

where ds is an infinitesimal line element, and k_{ab} and k_{sc} are the neutrino opacities for absorption and scattering, respectively. For the second, more emphasis is put on those inelastic processes that are effective in keeping neutrinos in thermal equilibrium with matter. In this case, we have

$$\mathrm{d}\tau_{\nu,\mathrm{en}} = \rho\sqrt{k_{\mathrm{ab}}\,(k_{\mathrm{sc}} + k_{\mathrm{ab}})}\,\mathrm{d}s, \tag{22}$$

where we have considered absorption processes as inelastic, and scattering processes as elastic.[4] The surfaces where τ_ν equals 2/3 are defined as *neutrino surfaces*. The neutrino surfaces obtained from $\tau_{\nu,\mathrm{sc}}$ can be understood as the *last scattering surfaces*; the ones derived from $\tau_{\nu,\mathrm{en}}$ correspond to the surfaces where neutrinos decouple thermally from matter, and they are often called *energy surfaces* (see e.g. Raffelt 2001). In Appendix A1, we describe the procedure adopted in our model to calculate the optical depths.

As a consequence of the distinction between emission and absorption processes, and between different neutrino species, the source terms in equations (17)–(19) can be split into different contributions. For the electron fraction,

$$\left(\frac{\mathrm{d}Y_{\mathrm{e}}}{\mathrm{d}t}\right)_\nu = -m_{\mathrm{b}}\left[\left(R^0_{\nu_{\mathrm{e}}} - R^0_{\bar{\nu}_{\mathrm{e}}}\right) + \left(H^0_{\nu_{\mathrm{e}}} - H^0_{\bar{\nu}_{\mathrm{e}}}\right)\right], \tag{23}$$

where R^0_ν and H^0_ν denote the specific particle emission and absorption rates for a neutrino type ν, respectively, and m_{b} is the baryon mass (with $m_{\mathrm{b}}c^2 = 939.021$ MeV). For the specific internal energy of the fluid,

$$\left(\frac{\mathrm{d}e}{\mathrm{d}t}\right)_\nu = -\left(R^1_{\nu_{\mathrm{e}}} + R^1_{\bar{\nu}_{\mathrm{e}}} + 4\,R^1_{\nu_{\mu,\tau}}\right) + H^1_{\nu_{\mathrm{e}}} + H^1_{\bar{\nu}_{\mathrm{e}}}, \tag{24}$$

where R^1_ν and H^1_ν indicate the specific energy emission and absorption rates, respectively. The factor 4 in front of $R^1_{\nu_{\mu,\tau}}$ accounts for the four different species modelled collectively as $\nu_{\mu,\tau}$. And, finally, for the fluid velocity,

$$\left(\frac{\mathrm{d}\boldsymbol{v}}{\mathrm{d}t}\right)_\nu = \left(\frac{\mathrm{d}\boldsymbol{v}}{\mathrm{d}t}\right)_{\nu_{\mathrm{e}}} + \left(\frac{\mathrm{d}\boldsymbol{v}}{\mathrm{d}t}\right)_{\bar{\nu}_{\mathrm{e}}} \tag{25}$$

is the acceleration provided by the momentum transferred by the absorption of ν_{e}s and $\bar{\nu}_{\mathrm{e}}$s in the optically thin region. Since the trapped neutrino component is not dynamically modelled, we neglect the related neutrino stress in optically thick conditions. As a consequence, $\nu_{\mu,\tau}$s do not contribute to the acceleration term.

The specific emission rates ($R^{0,1}_\nu$) are computed from smooth interpolations between the spectral production and diffusion rates. The former are expected to be relevant in optically thin conditions, the latter in opaque regions. On the other hand, the specific absorption rates in optically thin conditions (relevant for $H^{0,1}_\nu$ and $(\mathrm{d}\boldsymbol{v}/\mathrm{d}t)_\nu$) are obtained as a product between the local absorptivities

[3] The ASL scheme allows also the modelling of the neutrino-trapped component. However, since this component was not included in the study of the merger process that provided our initial conditions, we neglect it here.

[4] This is not true in general. However, it applies to the set of reactions we have chosen for our model; see Table 1.

and the neutrino particle densities. These densities are computed by a ray-tracing algorithm that takes, as radiation sources, the emission rates at the last scattering surfaces and above them. The details of these calculations are provided in Appendix A2.

For each neutrino ν species, the *luminosity* (L_ν) and *number luminosity* ($L_{N,\nu}$) are calculated as

$$L_\nu = \int_V \rho \left(R^1_\nu - H^1_\nu\right) \mathrm{d}V \tag{26}$$

and

$$L_{N,\nu} = \int_V \rho \left(R^0_\nu - H^0_\nu\right) \mathrm{d}V, \tag{27}$$

where V is the volume of the domain. The explicit distinction between the emission and the absorption contributions, as well as their dependence on the spatial position, allows the introduction of two supplementary luminosities.

1) The *cooling luminosities*,$L_{\nu,\mathrm{cool}}$ and $L_{N,\nu,\mathrm{cool}}$, obtained by neglecting the heating rates H^1_ν and H^0_ν in equations (26) and (27), respectively.

2) The *HMNS luminosities*,$L_{\nu,\mathrm{HMNS}}$ and $L_{N,\nu,\mathrm{HMNS}}$, obtained by restricting the volume integral in equations (26) and (27) to V_{HMNS}, the volume of the central object. Because of the continuous transition between the HMNS and the disc, the definition of V_{HMNS} is somewhat arbitrary. We decide to include also the innermost part of the disc, delimited by a density contour of 5×10^{11} g cm^{-3}. This corresponds to the characteristic density close to the innermost stable orbit for a torus accreting on stellar black holes. It is also comparable with the surface density of a cooling protoneutron star. For each luminosity we associate a *neutrino mean energy*, defined as $\langle E_\nu \rangle \equiv L_\nu / L_{N,\nu}$.

3.3 Initial conditions

The current study is based on previous, 3D hydrodynamic studies of the merger of two non-spinning 1.4 $\mathrm{M}_\odot$ neutron stars. This simulation was performed with a 3D SPH code, the implementation details of which can be found in the literature (Rosswog et al. 2000; Rosswog & Liebendörfer 2003; Rosswog 2005; Rosswog & Price 2007). For overviews over the SPH method, the interested reader is referred to recent reviews (Monaghan 2005; Rosswog 2009, 2014a,b; Springel 2010; Price 2012). The neutron star matter is modelled with the Shen et al. EoS (Shen et al. 1998a,b), and the profiles of the density and β-equilibrium electron fraction can be found in fig. 1 of Rosswog et al. (2013). During the merger process the debris can cool via neutrino emission, and electron/positron captures can change the electron fraction. These processes are included via the opacity-dependent, multiflavour leakage scheme of Rosswog & Liebendörfer (2003). Note, however, that no heating via neutrino absorption is included. Their effects are the main topic of the present study.

As the starting point of our neutrino-radiation hydrodynamics study, we consider the matter distribution of the 3D SPH simulation with 10^6 particles, at 15 ms after the first contact (corresponding to 18 ms after the simulation start). Not accounting for the neutrino absorption during this short time, should only have a small effect, since, according to the estimates from Section 2, the remnant hardly had time to change.

We map the 3D SPH matter distributions of density, temperature, electron fraction and fluid velocity on the Cartesian, equally spaced grid of FISH, with a resolution of 1 km. The initial extension of the grid is ($800 \times 800 \times 640\,\mathrm{km}^3$). During the simulation, we increase the domain in all directions to follow the wind expansion, keeping the HMNS always in the centre. At the end, the computational box is ($2240 \times 2240 \times 3360\,\mathrm{km}^3$) wide.

The initial data cover a density range of 10^8–3.5×10^{14} g cm^{-3}. Surrounding the remnant, we place an inert atmosphere, characterized by the following stationary properties: $\rho_{\mathrm{atm}} = 5 \times 10^3$ g cm^{-3}, $T_{\mathrm{atm}} = 0.1$ MeV, $Y_{\mathrm{e,atm}} = 0.01$ and $\boldsymbol{v}_{\mathrm{atm}} = \mathbf{0}$. The neutrino source terms are set to 0 in this atmosphere. With this treatment, we minimize the influence of the atmosphere on the disc and on the wind dynamics.

Even though in our model we try to stay as close as possible to the choices adopted in the SPH simulation, initial transients appear at the start of the simulation. One of the causes is the difference in the spatial resolutions between the two models. The resolution we are adopting in FISH is significantly lower than the one provided by the initial SPH model inside the HMNS, ∼0.125 km, (which is necessary to model consistently the central object), while it is comparable or better inside the disc. Because of this lack of resolution, we decide to treat the HMNS as a stationary rotating object. To implement this, we perform axisymmetric averages of all the hydrodynamical quantities at the beginning of the simulation. At the end of each hydrodynamical time step, we re-map these profiles in cells contained inside an ellipsoid, with $a_x = a_y = 30$ km and $a_z = 23$ km, and for which $\rho > 2 \times 10^{11}$ g cm^{-3}. For the velocity vector, we consider only the azimuthal component, since (1) the HMNS is rotating fast around its polar axis (with a period $P \approx 1.4$ ms) and (2) the non-azimuthal motion inside it is characterized by much smaller velocities (for example, $|v_R| \sim 10^{-3}|v_\phi|$, where v_R and v_ϕ are the radial and the azimuthal velocity components). Concerning the density and the rotational velocity profiles, our treatment is consistent with the results obtained by Dessart et al. (2009) (fig. 4), who showed that ∼100 ms after the neutron star have collided those quantities have changed only slightly inside the HMNS. We expect the electron fraction and the temperature also to stay close to their initial values, since the most relevant neutrino surfaces for ν_{e} and $\bar{\nu}_{\mathrm{e}}$ are placed outside the stationary region and the diffusion time-scale is much longer than the simulated time (see e.g. Section 2).

To give the opportunity to the system to adjust to a more stable configuration on the new grid, we consider the first 10 ms of the simulation as a 'relaxation phase'. During this phase, we evolve the system considering only neutrino emission. Its duration is chosen so that the initial transients arrive at the disc edge, and the profiles inside the disc reach new quasi-stationary conditions. The 'relaxed' conditions are visible in Fig. 2. They are considered as the new initial conditions and we evolved them for ∼90 ms, including the effect of neutrino absorption. In the following, the time t will be measured with respect to this second re-start. During the relaxation phase, we notice an increase of the electron fraction, from 0.05 up to 0.1–0.35, for a tiny amount of matter ($\lesssim 10^{-5}$ $\mathrm{M}_\odot$) in the low-density region ($\rho \lesssim 10^9$ g cm^{-3}) situated above the innermost, densest part of the disc ($R_{\mathrm{cyl}} \lesssim 50$ km, $|z| \gtrsim 20$ km). Here, the presence of neutron-rich, hot matter in optically thin conditions favours the emission of $\bar{\nu}_{\mathrm{e}}$, via positron absorption on neutrons. A similar increase of Y_{e} is also visible in the original SPH simulations, for times longer than 15 ms after the first collision.

In Fig. 3 we show isocontours of the absolute value of gravitational specific energy, drawn against the colour-coded matter density, at the beginning of our simulation. The gravitational energy provides an estimate of the energy that neutrinos have to deposit to unbound matter, at different locations inside the disc (see Section 2).

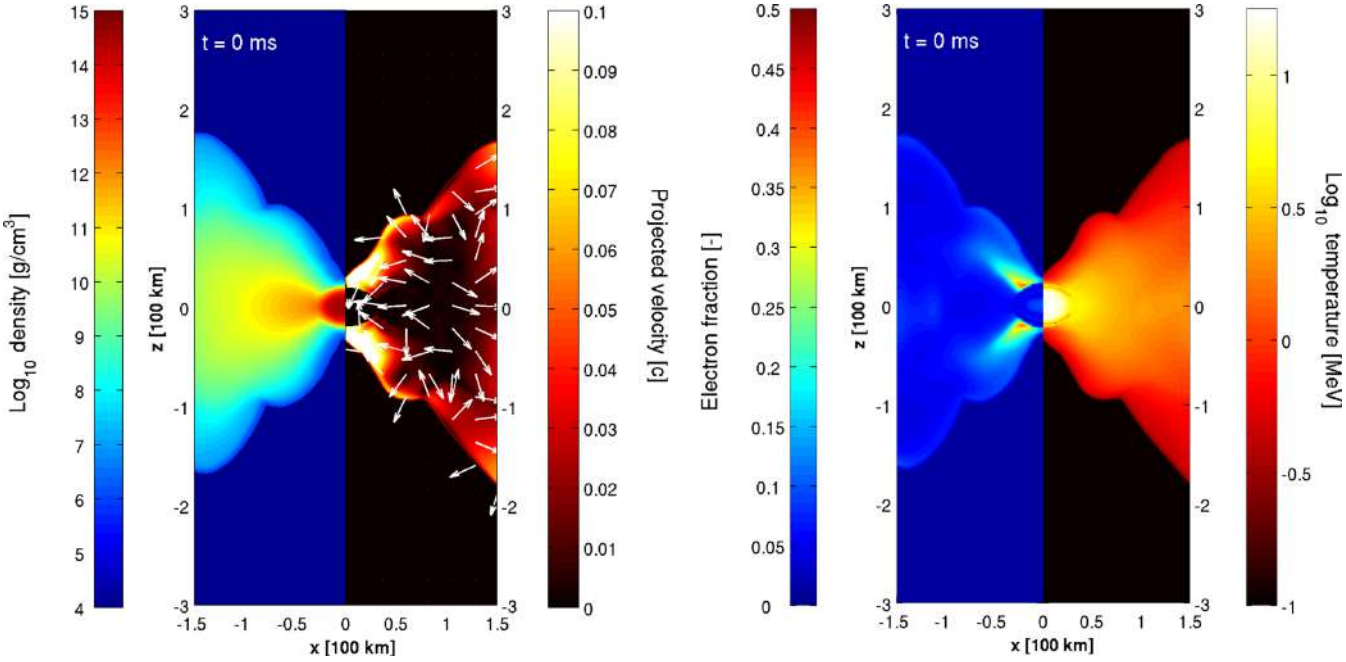

Figure 2. Vertical slices of the 3D domain (corresponding to the $y = 0$ plane), recorded at the beginning of the simulation. In the left-hand panel, we colour coded the logarithm of the matter density (in g cm^{-3}, left-hand side) and the projected fluid velocity (in units of c, on the right-hand side); the arrows indicate the direction of the projected velocity in the plane. On the right-hand panel, we represent the electron fraction (left-hand side) and the logarithm of the matter temperature (in unit of MeV, right-hand side).

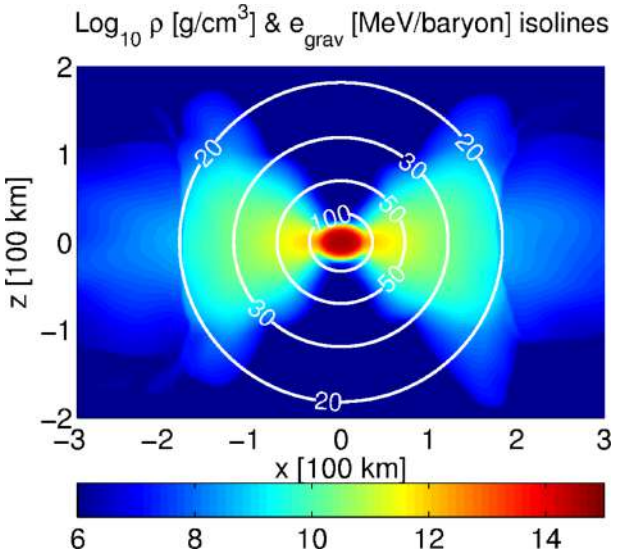

Figure 3. Logarithm of the matter density (colour coded, in g cm^{-3}) and isocontours of the gravitational energy (white lines, in MeV baryon^{-1}), on a vertical slice of the 3D domain, at $t = 0$.

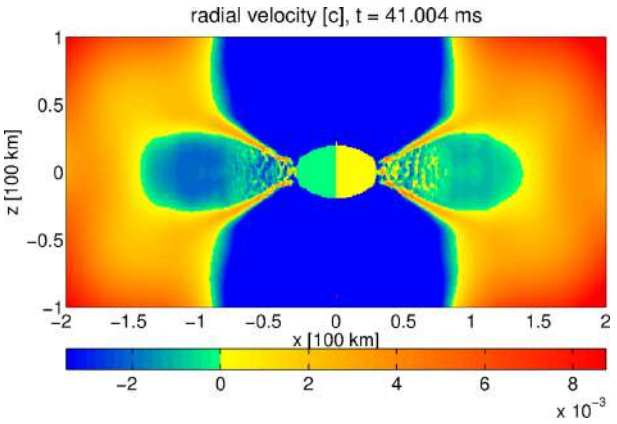

Figure 4. Vertical slice of the inner part of the 3D domain ($y = 0$ plane), taken at 41 ms after the beginning of the simulations. Colour coded is the radial component of the fluid velocity. The two coloured hemispheres in the centre represent the stationary central object for which $v_r \approx 0$ (the two actual colours are very small numbers).

4 SIMULATION RESULTS

4.1 Disc evolution and matter accretion

After the highly dynamical merger phase, the remnant is still dynamically evolving and not yet in a perfectly stationary state.

In Fig. 4, we show the radial component of the fluid velocity on the $y = 0$ plane, at 41 ms after the beginning of the simulation. The central part of the disc, corresponding to a density contour of $\sim 5 \times 10^9$ g cm^{-3}, is slowly being accreted on to the HMNS ($v_R \sim$ a few $10^{-3}c$), while the outer edge is gradually expanding along the equatorial direction. The velocity profile shows interesting asymmetries and deviations from an axisymmetric behaviour. The surface of the HMNS and the innermost part of the disc are characterized by steep gradients of density and temperature, and they behave like a pressure wall for the infalling matter. Outgoing sound waves are then produced and move outwards inside the disc, transporting energy, linear and angular momentum. At a cylindrical radius of $R_{\rm cyl} \lesssim 80$ km, they induce small-scale perturbations in the velocity field, visible as bubbles of slightly positive radial velocity. These perturbations dissolve at larger radii, releasing their momentum and energy inside the disc, and favouring its equatorial expansion.

The temporal evolution of the accretion rate $\dot{M}$, computed as the net flux of matter crossing a cylindrical surface of radius

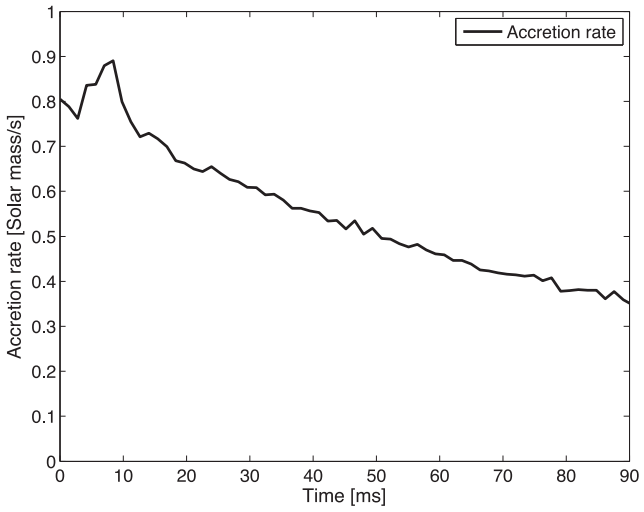

Figure 5. Temporal evolution of the accretion rate on the HMNS, $\dot{M}$, calculated as the net flux of matter crossing a cylindrical surface of radius $R_{\rm cyl} = 35$ km and axis corresponding to the rotational axis of the disc.

$R_{\rm cyl} = 35$ km and axis corresponding to the rotational axis of the disc, is plotted in Fig. 5. This accretion rate is compatible with the estimate performed in Section 2 using an α-viscosity disc model. A direct comparison with equation (3) suggests an effective parameter $\alpha \approx 0.05$ for our disc. We stress again that no physical viscosity is included in our model: the accretion is driven by unbalanced pressure gradients, neutrino cooling (see Section 4.2) and dissipation of numerical origin. However, the previous estimate is useful to compare our disc with purely Keplerian discs, in which a physical α-viscosity has been included (usually, with $0.01 \lesssim \alpha \lesssim 0.1$). Our value of $\alpha \approx 0.05$ is close to what is usually assumed for such discs ($\sim$0.1). Higher viscosities would enhance the neutrino emission and probably the mass loss.

On a time-scale of a few tens of milliseconds, the profiles inside the disc change, as consequence of the accretion process and of the outer edge expansion. These effects are visible in the upper row of Fig. 6, where radial profiles of temperature and density are drawn, at different times and heights inside the disc. We notice, in particular, that the density decreases in the internal part of the disc ($50 \lesssim R_{\rm cyl} \lesssim 200$ km), as result of the accretion. In the same region, the balance between the increase of internal energy and the efficient cooling provided by neutrino emission keeps the temperature almost stationary. At larger radial distances ($R_{\rm cyl} \gtrsim 200$ km), the initial accretion of a cold, thin layer of matter (visible in the $t = 2$ ms profiles) is followed by the continuous expansion of the outer margin of the hot internal disc.

4.2 Neutrino emission

In Fig. 7, we show the neutrino surfaces obtained by the calculation of the spectral neutrino optical depths, together with the matter density distribution (axisymmetric, colour coded). Different lines correspond to different energy bins. In the upper panels, we represent the scattering neutrino surfaces, while in the lower panels the energy ones. Their shapes follow closely the matter density distribution, due to the explicit dependence appearing in equations (21) and (22). The last scattering surfaces for the energies that are expected to be more relevant for the neutrino emission ($10 \lesssim E_\nu \lesssim 25$ MeV, corresponding to the expected range for the mean energies, as we will discuss below) extend far outside in the disc, compared with the radius of the central object. $\nu_{\rm e}$s have the largest opacities, due to the extremely neutron-rich environment that favours processes

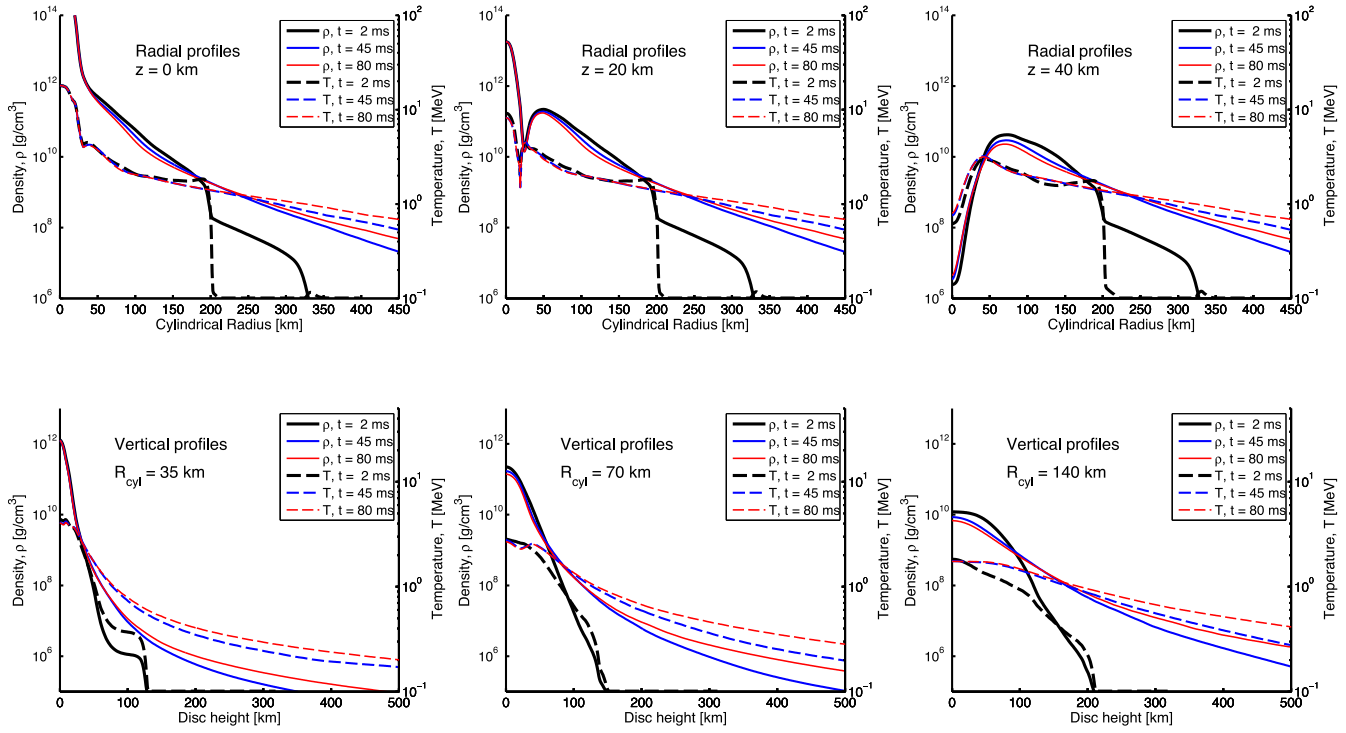

Figure 6. Radial (upper row) and vertical (lower row) profiles of the axisymmetric density (solid lines) and temperature (dashed lines) inside the disc, recorded at different times during the simulation [$t \approx 2$ ms (black thick lines), $t \approx 45$ ms (blue normal lines), $t \approx 80$ ms (red thin lines)]. The different columns correspond to different values of the section coordinates: from left to right, $z = 0, 20, 40$ km for the radial profiles; $R_{\rm cyl} = 35, 70, 140$ km for the vertical ones.

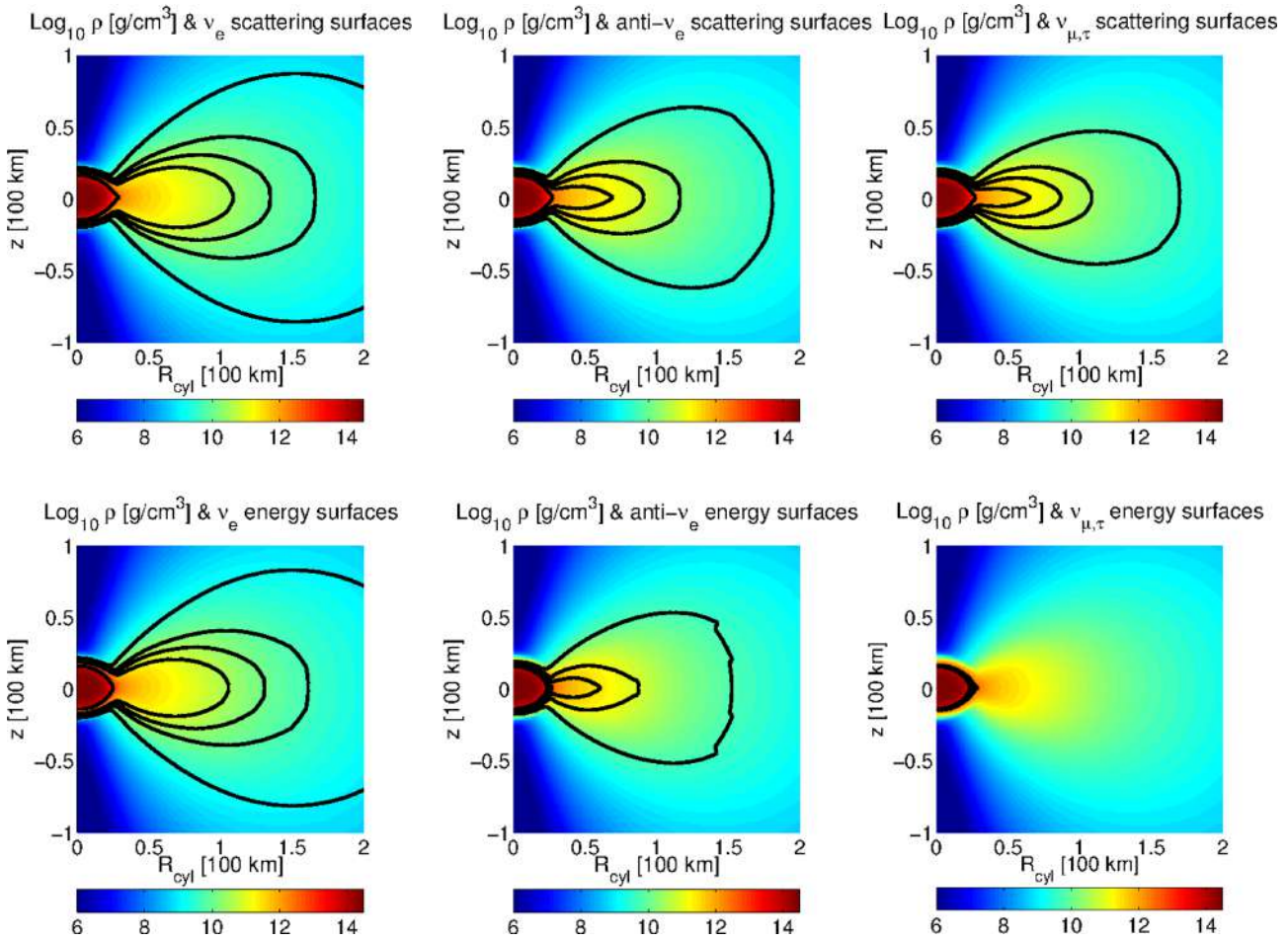

Figure 7. Location of the neutrino surfaces for ν_e (left-hand column), $\bar{\nu}_e$ (central column) and $\nu_{\mu,\tau}$ (right-hand column), for the scattering optical depth (upper row) and for the energy optical depth (bottom row), 40 ms after the beginning of the simulation. Colour coded is the logarithm of cylindrically averaged matter density, ρ (g cm^{-3}). The different lines correspond to the neutrino surfaces for different values of the neutrino energy: from the innermost line to the outermost one, $E_\nu = 4.62, 10.63, 16.22, 24.65, 56.96$ MeV.

like neutrino absorption on neutrons. Since the former reaction is also very efficient in thermalizing neutrinos, the scattering and the energy neutrino surfaces are almost identical for ν_es. In the case of $\bar{\nu}_e$s, the relatively low density of free protons determines the reduction of the scattering and, even more, of the energy optical depth. For $\nu_{\mu,\tau}$s, neutrino bremsstrahlung and $e^+ - e^-$ annihilation freeze out at relatively high densities and temperatures ($\rho \sim 10^{13}$ g cm^{-3} and $k_B T \sim 8$ MeV), reducing further the energy neutrino surfaces, while elastic scattering on nucleons still provides a scattering opacity comparable to the one of $\bar{\nu}_e$s.

The energy- and volume-integrated luminosities obtained during the simulation are presented in Fig. 8. The cooling luminosities for ν_es and $\bar{\nu}_e$s (dashed lines) decrease weakly and almost linearly with time. This behaviour reflects the continuous supply of hot accreting matter. The faster decrease of $\dot{M}$ (cf. Fig. 5) would imply a similar decrease in the luminosities, if the neutrino radiative efficiency of the disc were constant. However, the latter increases with time due to the decrease of density and the constancy of temperature characterizing the innermost part of the disc (see Section 4.1). Also the luminosity for the $\nu_{\mu,\tau}$ species is almost constant. This is a consequence of the stationarity of the central object, since most of the $\nu_{\mu,\tau}$s come from there. However, this result is compatible with the long cooling time-scale of the HMNS, equation (6). We specify here that the plotted lines for $\nu_{\mu,\tau}$ correspond to one single species. Thus, the *total* luminosity coming from heavy flavour neutrinos is four times the plotted one, see also equation (24).

In the case of ν_es and $\bar{\nu}_e$s, the luminosity provided by $V_{\rm HMNS}$ (defined in Section 3.2 and represented by dot–dashed lines in Fig. 8) and the luminosity of the accreting disc are comparable. This result is compatible with what is observed in core collapse supernova simulations (see e.g. fig. 6 of Liebendörfer et al. 2005), a few tens of milliseconds after bounce: assuming a density cut of 5×10^{11} g cm^{-3} for the protoneutron star, its contribution is roughly half of the total emitted luminosity, for both ν_e and $\bar{\nu}_e$. Instead, if we further restrict $V_{\rm HMNS}$ only to the central ellipsoid (see Section 3.3 for more details), we notice that the related luminosity reduces to $\lesssim 10 \times 10^{51}$ erg s^{-1} for all neutrino species. This is consistent with our preliminary estimate, equation (7).

The inclusion of neutrino absorption processes in the optically thin region reduces the cooling luminosities to the net luminosities (solid lines in Fig. 8). For ν_es, the neutron-rich environment reduces the number luminosity by ≈37 per cent, while for $\bar{\nu}_e$s this fraction drops to ≈14 per cent.

The values of the neutrino mean energies are practically stationary during the simulation: from the net luminosities at $t \approx 40$ ms, $\langle E_{\nu_e} \rangle \approx 10.6$ MeV, $\langle E_{\bar{\nu}_e} \rangle \approx 15.3$ MeV and $\langle E_{\nu_{\mu,\tau}} \rangle \approx 17.3$ MeV. The mean neutrino energies show the expected hierarchy, $\langle E_{\nu_e} \rangle < \langle E_{\bar{\nu}_e} \rangle < \langle E_{\nu_{\mu,\tau}} \rangle$, reflecting the different locations of the thermal

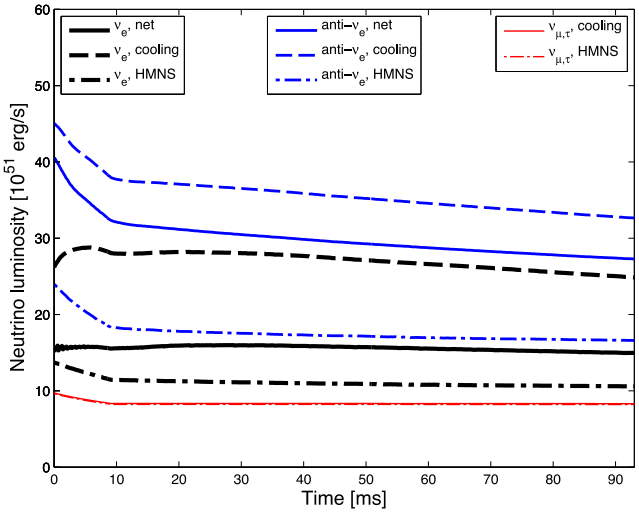

Figure 8. Time evolution of the net (solid) and cooling (dashed) luminosities obtained by the ASL scheme for ν_e (black thick), $\bar{\nu}_e$ (blue normal) and $\nu_{\mu,\tau}$ (red thin) neutrino species. The difference between the cooling and the net luminosities is represented by the re-absorbed luminosity. The contributions to the cooling luminosities coming from the HMNS, defined as the volume characterized by $\rho > 5 \times 10^{11}$ g cm^{-3}, are also plotted (dot–dashed lines). Note that for $\nu_{\mu,\tau}$, the net and the cooling luminosities coincide, and they are almost equal to the HMNS contribution.

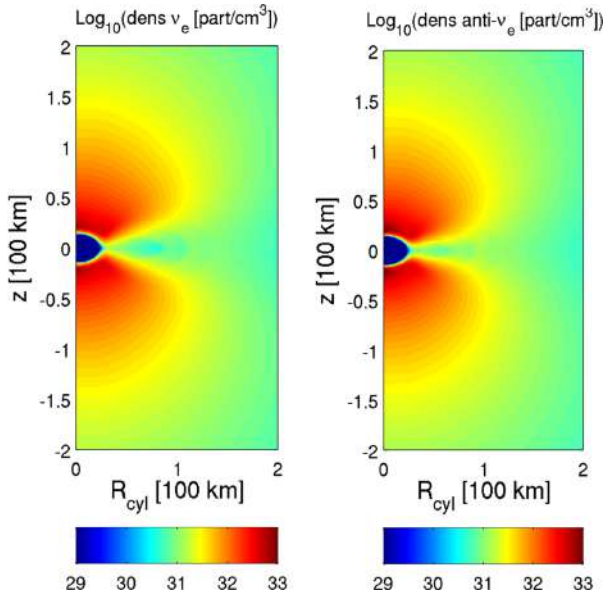

Figure 9. Energy-integrated (axisymmetric) neutrino density of the free-streaming neutrinos, N_ν, for ν_e (left-hand panel) and $\bar{\nu}_e$ (right-hand panel), calculated outside the innermost neutrino surface (corresponding to $E_\nu = 3$ MeV), at $t \approx 40$ ms after the beginning of the simulation.

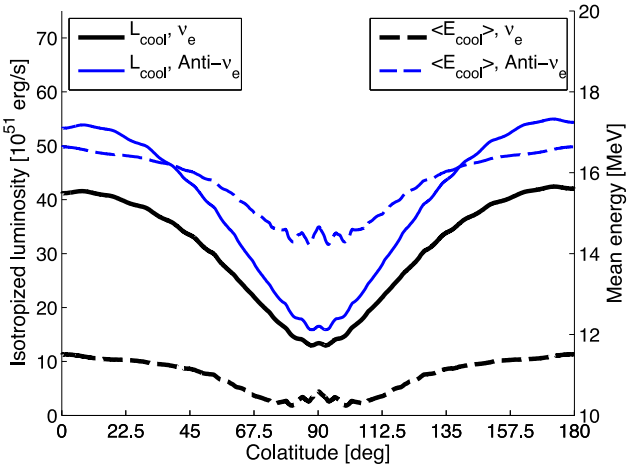

Figure 10. Angular dependence of the isotropized neutrino cooling luminosities (solid line) and of the neutrino mean energies (dashed lines), as a function of the colatitude. The black thick lines correspond to ν_e, while the blue thin lines to $\bar{\nu}_e$. As a representative time, we consider $t \approx 40$ ms after the beginning of the simulation.

decoupling surfaces. While the values obtained for ν_es and $\bar{\nu}_e$s are consistent with previous calculations, $\langle E_{\nu_{\mu,\tau}} \rangle$ is smaller than expected (see e.g. Rosswog et al. 2013). This is due to the lack of resolution at the HMNS surface, where most of the energy neutrino surfaces for $\nu_{\mu,\tau}$ are located. This discrepancy has no dynamical effects for us, since most of $\nu_{\mu,\tau}$ come from the stationary central object.

The ray-tracing algorithm, see Appendix A2, allows us to compute (1) the neutrino densities outside the neutrino surfaces; (2) the angular distribution of the isotropized neutrino cooling luminosities and mean neutrino energies, as seen by a far observer. In Fig. 9, we represent the energy-integrated axisymmetric neutrino densities N_ν, equation (A11), for ν_e (left) and $\bar{\nu}_e$ (right). These densities reach their maximum in the funnel above the HMNS due to the geometry of the emission and to the short distance from the most emitting regions. At distances much larger than the dimension of the neutrino surfaces, N_ν shows the expected R^{-2} dependence.

The disc geometry introduces a clear anisotropy in the neutrino emission, visible in Fig. 10. Because of the larger opacity along the equatorial direction, the isotropic luminosity along the poles is ∼3–3.5 more intense than the one along the equator. The different temperatures at which neutrinos decouple from matter at different polar angles determine the angular dependence of the mean energies.

4.3 Neutrino-driven wind

The evolution of the disc and the formation of a neutrino-driven wind depend crucially on the competition between neutrino emission and absorption. In Fig. 11, we show axisymmetric averages of the net specific energy rate (left), of the net electron fraction rate (centre) and of the acceleration due to neutrino absorption (right), at $t = 40$ ms.

Inside the most relevant neutrino surfaces and a few kilometres outside them, neutrino cooling dominates. Above this region, neutrino heating is always dominant. The largest neutrino heating rate happens in the funnel, where the neutrino densities are also larger. However, these regions are characterized by matter with low density ($\rho \lesssim 10^7$ g cm^{-3}) and small specific angular momentum. Thus, this energy deposition has a minor dynamical impact on this rapidly accreting matter. On the other hand, at larger radii ($80 \lesssim R_{cyl} \lesssim 120$ km) net neutrino heating affects denser matter ($\rho \lesssim 10^{10}$ g cm^{-3}), rotating inside the disc around the HMNS. This combination provides an efficient net energy deposition.

Neutrino diffusion from the optically thick region determines small variations around the initial weak equilibrium value in the electron fraction. On the contrary, in optically thin conditions, the initial very low electron fraction favours reactions like the absorption of e^+ and ν_e on free neutrons. Both processes lead to

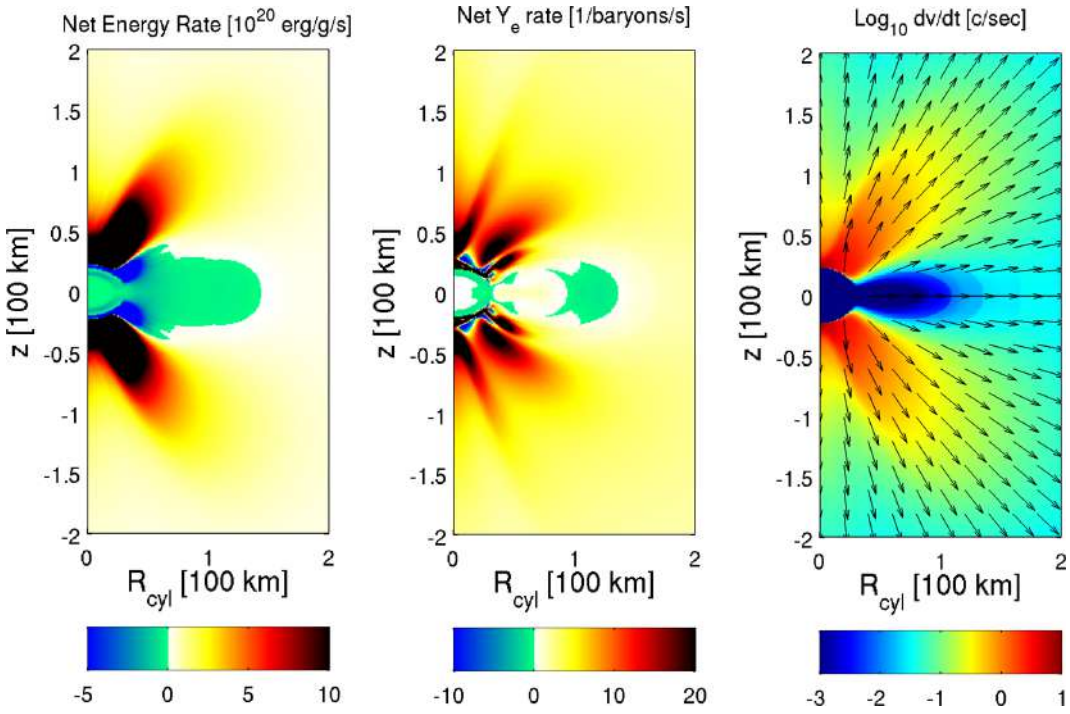

Figure 11. Energy- and species-integrated axisymmetric ν net rates for energy (left-hand panel, in units of 10^{20} erg g^{-1} s^{-1}) and Y_e (central panel, in units of 1 baryon^{-1} s^{-1}), and of the fluid velocity variation provided by neutrino absorption in the optically thin regions (right-hand panel, in units of $c\,$s^{-1}). As a representative time, we consider $t \approx 40$ ms after the beginning of the simulation. The complex structure of the net Y_e rate in the funnel, above the HMNS poles, originates from the variety of conditions of Y_e, ρ and $\boldsymbol{v}$ at that specific moment.

a positive and large $(\mathrm{d}Y_e/\mathrm{d}t)_\nu$, in association with efficient energy deposition.

Because of the geometry of the emission and to the shadow effect provided by the disc, the direction of the acceleration provided by neutrino absorption is approximately radial, but its intensity is much larger in the funnel, where the energy deposition is also more intense.

As a consequence of the continuous neutrino energy and momentum deposition, the outer layers of the disc start to expand a few milliseconds after the beginning of the simulation, and they reach an almost stable configuration in a few tens of milliseconds. Around $t \sim 10$ ms, also the neutrino-driven wind starts to develop from the expanding disc. Wind matter moves initially almost vertically (i.e. with velocities parallel to the rotational axis of the disc), decreasing its density and temperature during the expansion. We show the corresponding vertical profiles inside the disc in the bottom panels of Fig. 6, at different times and for three cylindrical radii. Both the disc and the wind expansions are visible in the rise of the density and temperature profiles, especially at cylindrical radii of 70 and 140 km.

Among the energy and the momentum contributions, the former is the most important one for the formation of the wind. To prove this, we repeat our simulation in two cases, starting from the same initial configuration and relaxation procedure. In a first case, we set the heating rate h_ν appearing in equations (A3) and (A4) to 0. Under this assumption, we observe neither the disc expansion nor the wind formation. In a second test, we include the effect of neutrino absorption only in the energy and Y_e equations, but not in the momentum equation. In this case, the wind still develops and its properties are qualitatively very similar to our reference simulation.

In Figs 12–14 we present three different times of the wind expansion, $t = 20, 40, 85$ ms. To characterize them, we have chosen vertical slices of the 3D domain, for the density and the projected velocity (left-hand picture), and for the electron fraction and the matter entropy (right-hand picture).

The development of the wind is clearly associated with the progressive increase of the electron fraction. The resulting Y_e distribution is not uniform, due to the competition between the wind expansion time-scale (equation 12) and the time-scale for weak equilibrium to establish. The latter can be estimated as $t_{\rm weak} \sim Y_{\rm e,eq}/(\mathrm{d}Y_e/\mathrm{d}t)_\nu$. Using the values of the neutrino luminosities, mean energies and net rates for the wind region, we expect $Y_{\rm e,eq} \approx 0.42$ (see e.g. equation 77 of Qian & Woosley 1996) and $0.042 \lesssim t_{\rm weak} \lesssim 0.090$ s. If we keep in mind that the absorption of neutrinos becomes less efficient as the distance from the neutrino surfaces increases, we understand the presence of both radial and vertical gradients for Y_e inside the wind: the early expanding matter has not enough time to reach $Y_{\rm e,eq}$, especially if it is initially located at large distances from the relevant neutrino surfaces ($R_{\rm cyl} \gtrsim 100$ km). On the other hand, matter expanding from the innermost part of the disc and moving in the funnel (within a polar angle $\lesssim 40^\circ$), as well as matter that orbits several times around the HMNS before being accelerated in the wind, increases its Y_e close to the equilibrium value, but on a longer time-scale.

Also the matter entropy in the wind rises due to neutrino absorption. Typical initial values in the disc are $s \sim 5$–$10\,k_{\rm B}$ baryon^{-1}, while later we observe $s \sim 15$–$20\,k_{\rm B}$ baryon^{-1}. The entropy is usually larger where the absorption is more intense and Y_e has increased more. However, differently from Y_e, its spatial distribution is more uniform. Once the distance from the HMNS and the disc has increased above $\sim$400 km, neutrino absorption becomes negligible and the entropy and the electron fraction are simply advected inside the wind.

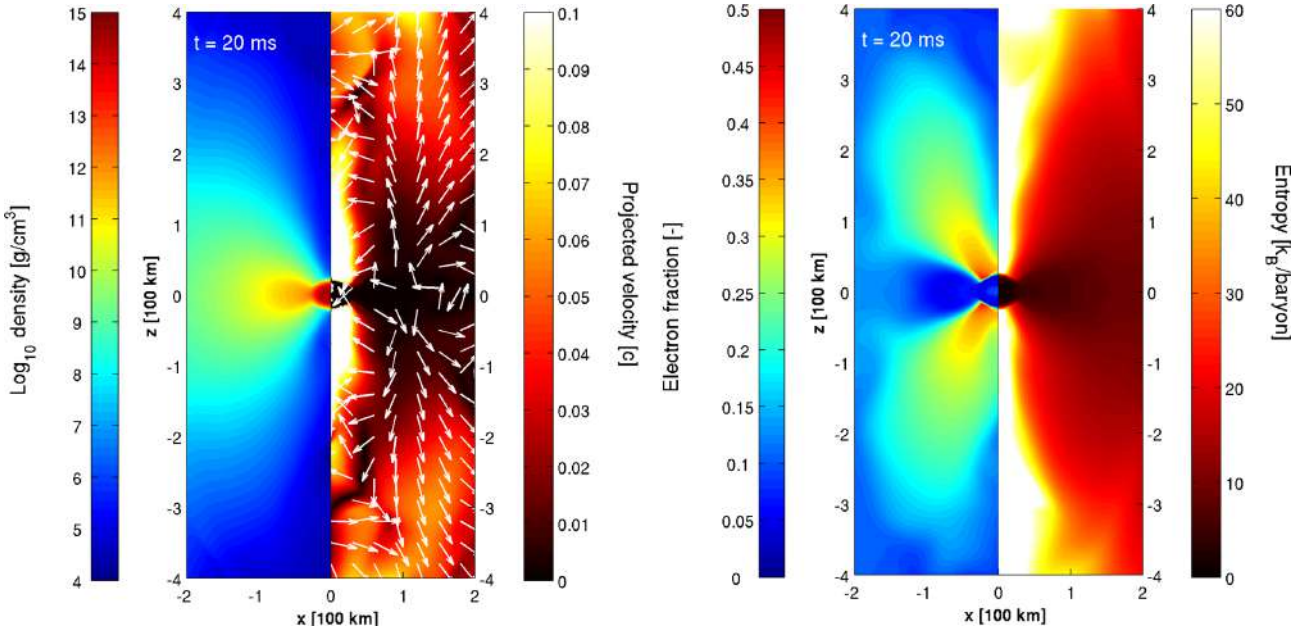

Figure 12. Vertical slices of the 3D domain (corresponding to the $y = 0$ plane), recorded 20 ms after the beginning of the simulation. In the left-hand panel, we represent the logarithm of the matter density (in g cm^{-3}, left-hand side) and the projected fluid velocity (in units of c, on the right-hand side); the arrows indicate the direction of the projected velocity in the plane. On the right-hand panel, we represent the electron fraction (left-hand side) and the matter entropy (in unit of k_B baryon^{-1}, right-hand side).

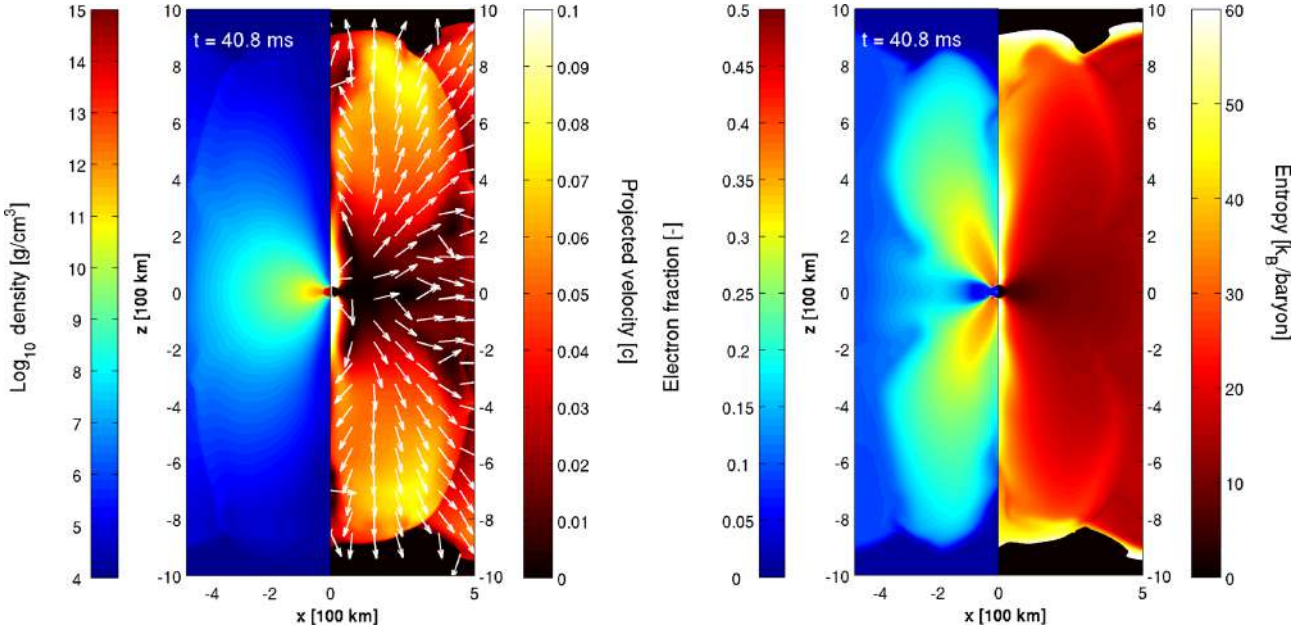

Figure 13. Same as in Fig. 12, but at ≈40 ms after the beginning of the simulation.

The radial velocity in the wind increases from a few times 10^{-2} c, just above the disc, to a typical asymptotic expansion velocity of 0.08–0.09 c. This acceleration is caused by the continuous pressure gradient provided by newly expanding layers of matter.

To characterize the matter properties, we plot in Fig. 15 2D mass histograms for couples of quantities, namely ρ–Y_e (top row), ρ–s (central row) and Y_e–s (bottom row), at three different times ($t = 0, 40, 85$ ms). Colour coded is a measure of the amount of matter experiencing specific thermodynamical conditions inside the whole system, at a certain time.[5]

We notice that most of the matter is extremely dense ($\rho > 10^{11}$ g cm^{-3}), neutron rich ($Y_e < 0.1$) and, despite the

[5] A formal definition of the plotted quantity can be found in section of Bacca et al. (2012). However, in this work we do not calculate the time average.

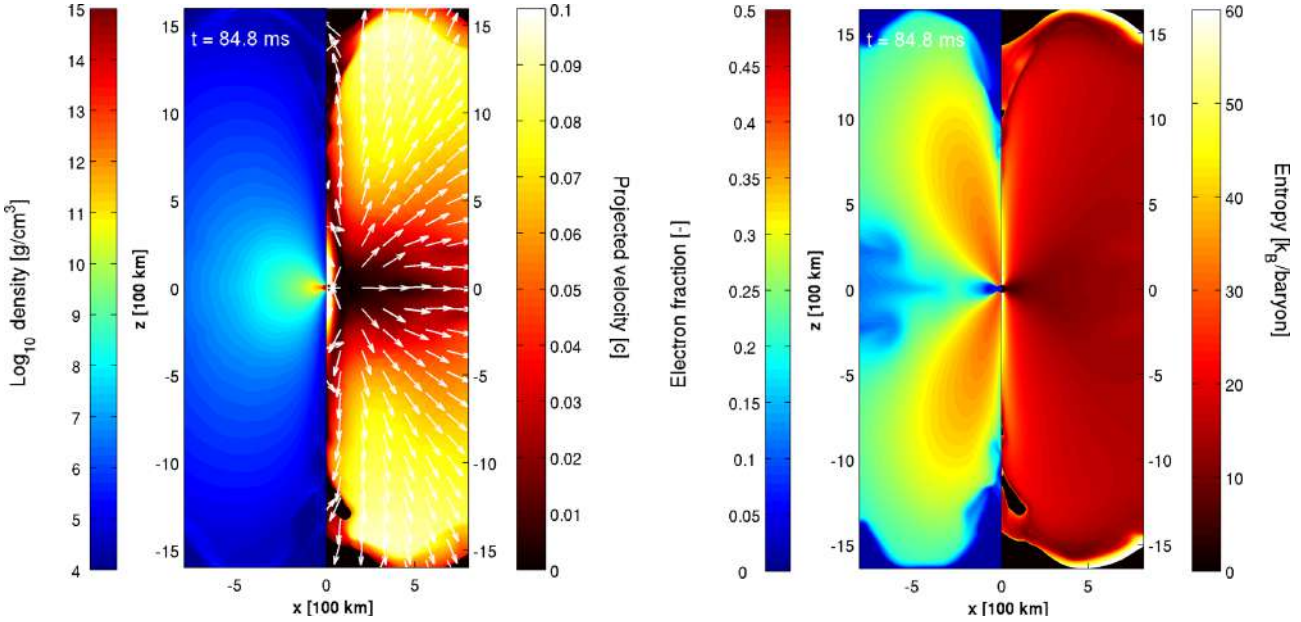

Figure 14. Same as in Fig. 12, but at ≈85 ms after the beginning of the simulation.

large temperatures ($T > 1$ MeV), at relatively low entropy ($s < 7\,k_B$ baryon^{-1}). This matter corresponds to the HMNS and to the innermost part of the disc, where matter conditions change only on the long neutrino diffusion time-scale, equation (6), or on the disc lifetime, equation (2). In the low-density part of the diagrams ($\rho < 10^{11}$ g cm^{-3}), the expansion of the disc and the development of the wind can be traced.

In Figs 16(a–d), we represent the mass fractions of the nuclear species provided by the nuclear EoS inside the disc and the wind, at 40 ms after the beginning of the simulation. Close to the equatorial plane ($|z| < 100$ km), the composition is dominated by free neutrons. In the wind, the increase of the electron fraction corresponds to the conversion of neutrons into protons due to ν_e absorption. In the early expansion phase, the relatively high temperature ($T \gg 0.6$ MeV) favours the presence of free protons. When the decrease of temperature allows the formation of nuclei, protons cluster into α particles and, later, into neutron-rich nuclei. Then, the composition in the wind, at large distances from the disc, is distributed between free neutrons ($0.4 \lesssim X_n \lesssim 0.6$) and heavy nuclei ($0.6 \gtrsim X_h \gtrsim 0.4$, respectively). The heavy nuclei component is described in the EoS by a representative average nucleus, assuming nuclear statistical equilibrium (NSE) everywhere. In Figs 16(e) and (f), we have represented the values of its mass and charge number. The most representative nucleus in the wind corresponds often to ^{78}Ni. The black line defines the surface across which the freeze-out from NSE is expected to occur ($T = 0.5$ MeV). Outside it the actual composition will differ from the NSE prediction (see Section 5).

4.4 Ejecta

Matter in the wind can gain enough energy from the neutrino absorption and from the subsequent disc dynamics to become unbound. The amount of ejected matter is calculated as volume integral of the density and fulfils three criteria: (1) has positive radial velocity; (2) has positive specific total energy; (3) lies inside one of the two cones of opening angle 60°, vertex in the centre of the HMNS and axes coincident with the disc rotation axes. The latter geometrical constraint excludes possible contributions coming from equatorial ejecta, which have not been followed properly during their expansion. The profile of Y_e at the end of the simulation (see e.g. Fig. 14) suggests to further distinguish between two zones inside each cone, one at high (H: $0° \leq \theta < 40°$, where θ is the polar angle) and one at low (L: $40° \leq \theta < 60°$) latitudes.

The specific total internal energy is calculated as

$$e_{tot} = e_{int} + e_{grav} + e_{kin}, \quad (28)$$

where e_{grav} is the Newtonian gravitational potential, and e_{kin} is the specific kinetic energy. The specific internal energy e_{int} takes into account the nuclear recombination energy and, to compute it, we use the composition provided by the EoS. For the nuclear binding energy of the representative heavy nucleus, we use the semi-empirical nuclear mass formula (see e.g. the fitting to experimental nuclei masses reported by Rohlf 1994): in the wind, for $\langle A \rangle \approx 78$ and $\langle Z \rangle \approx 28$, the nuclear binding energy is ∼8.1 MeV baryon^{-1}.

At the end of the simulation, $M_{ej}(t = 91\,\text{ms}) \approx 2.12 \times 10^{-3}$ M$_\odot$, corresponding to ∼1.2 per cent of the initial disc mass ($M_{disc} \approx 0.17$ M$_\odot$). This mass is distributed between $M_{ej,H}(t = 91\,\text{ms}) \approx 1.3 \times 10^{-3}$ M$_\odot$ at high latitudes and $M_{ej,L}(t = 91\,\text{ms}) \approx 0.8 \times 10^{-3}$ M$_\odot$ at low latitudes. In Fig. 17, we represent the mass distributions of density, electron fraction, entropy and radial velocity, for the ejecta at the end of our simulation. At high latitude, the larger ν_e absorption enhances the electron fraction and the entropy more than at lower latitudes. The corresponding mass distributions are broader, with peaks at $Y_e \sim 0.31$–0.35 and $s \sim 15$–$20 k_B$ baryon^{-1}. At lower latitudes, the electron fraction presents a relatively uniform distribution between 0.23 and 0.31, while the entropy has a very narrow peak around 14–15 k_B baryon^{-1}. The larger energy and momentum depositions produce a faster expansion of the wind close to the poles. This effect is visible in the larger average value and in the broader distribution of the radial velocity that characterizes the high-latitude ejecta.

To quantify the uncertainties in the determination of the ejecta mass, we repeat the previous calculation assuming an error of 0.5 MeV in the estimate of the nuclear recombination energy. For $M_{ej,H}$ this translates in an uncertainty of ≈7 per cent, while in the case of $M_{ej,L}$ the potential error is much larger (∼50 per cent). This

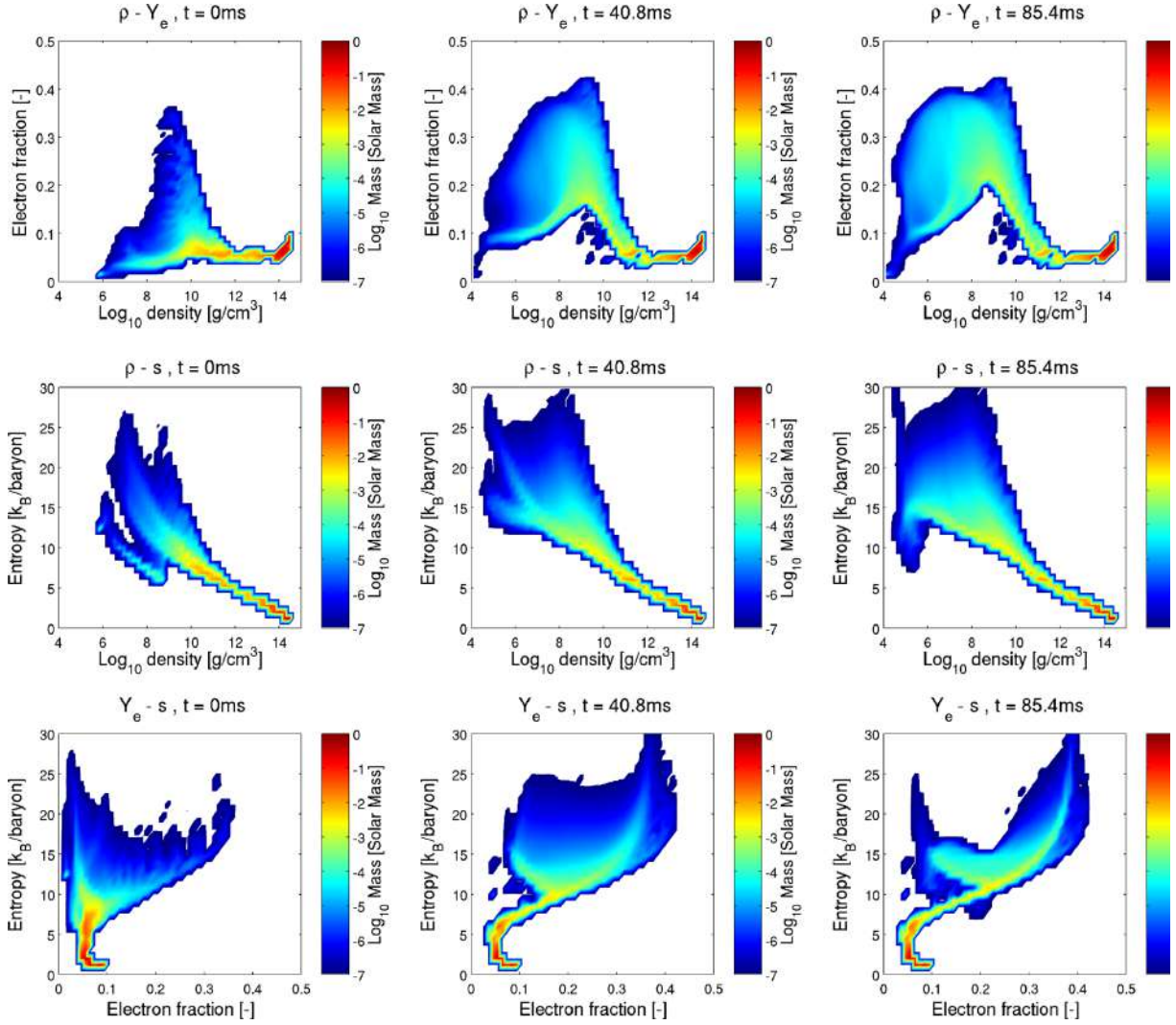

Figure 15. 2D mass histograms for (ρ, Y_e) (top panel), (ρ, s) (middle panels) and (Y_e, s) (bottom panels), for the thermodynamical properties of matter in the whole system, at $t \approx 0$ ms (left-hand column), $t \approx 40$ ms (central column) and $t \approx 85$ ms (right-hand column) after the beginning of the simulation. Colour coded is a measure of the amount of matter experiencing specific thermodynamical conditions inside the whole system. Values smaller than 10^{-7} $M_\odot$ have been omitted from the plot.

is a consequence of the different ejecta properties. At high latitudes, most of the free neutrons have been incorporated into heavy nuclei, releasing the corresponding binding energy. Moreover, the large radial velocities ($v_r \sim 0.08$–$0.09\,c$) provides most of the energy needed to overcome the gravitational potential. At lower latitudes, the more abundant free neutrons and the lower radial velocities ($v_r \sim 0.06$–$0.07\,c$) translate into a smaller ejecta amount, with a larger dependence on the nuclear recombination energy. Generally, we consider our numbers for the wind ejecta as lower limits, since (a) we ignore the presence and likely amplification of magnetic fields which could substantially enhance the mass loss (Thompson 2003), (b) so far, we ignore heating from neutrino-annihilation and (c) we do not consider colatitudes $>60^\circ$.

5 DISCUSSION

5.1 Comparison with previous works

The hierarchies we have obtained for the neutrino luminosities and mean energies agree with previous studies on the neutrino emission from neutron star mergers and their aftermaths. In the case of Newtonian simulations, the compatibility is good also from a quantitative point of view, usually within 25 per cent (see e.g. the values obtained in Rosswog et al. 2013, for the run H, to be compared with our cooling luminosities). On the other hand, general relativistic simulations (usually limited in time to the first tens of milliseconds after the merger) obtain larger neutrino luminosities (up to a factor of 2 or 3) due to larger matter temperatures and stronger shocks (see e.g. Sekiguchi et al. 2011; Kiuchi et al. 2012; Neilsen et al. 2014). The higher temperatures reduce also the ratio between $\bar{\nu}_e$ and ν_e luminosities, since the difference between charged current reactions on neutrons and protons diminishes ($k_B T \gg Q$), and thermal pair processes are enhanced.

Dessart et al. (2009) studied the formation of the neutrino-driven wind, starting from initial conditions very similar to ours, in axisymmetric simulations that employ a multigroup flux limited diffusion scheme for neutrinos. Our results agree with theirs concerning typical values of the neutrino luminosities and mean energies (with the exception of $\langle E_{\nu_{\mu,\tau}} \rangle$, see Section 4.2), as well as their angular distributions. Also the shape and the extension of the neutrino surfaces

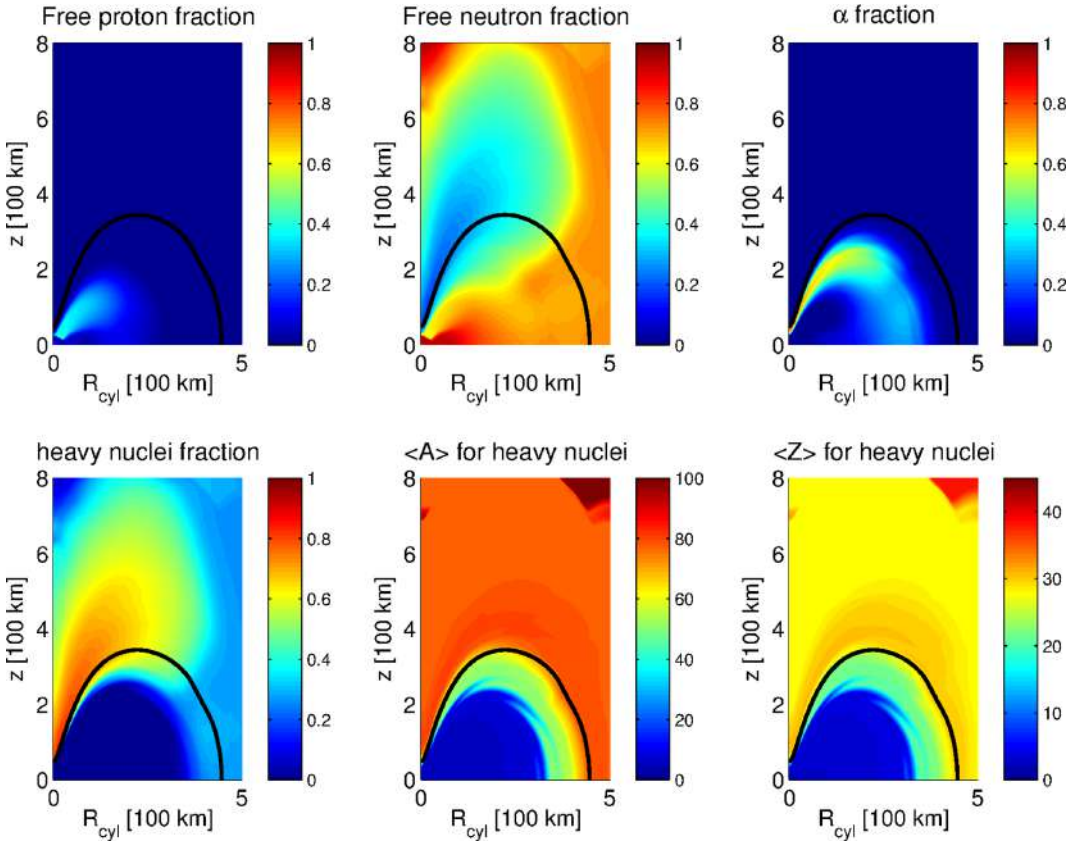

Figure 16. Nuclear composition provided by the EoS (assuming everywhere NSE) in the disc and in the wind, at $t \approx 40$ ms. On the top row, free proton (left), free neutron (centre) and α particles (right) mass fractions. On the bottom row, heavy nuclei mass fraction (left), mass number (centre) and atomic number (right) of the representative heavy nucleus. The black line represents the $T = 0.5$ MeV surface.

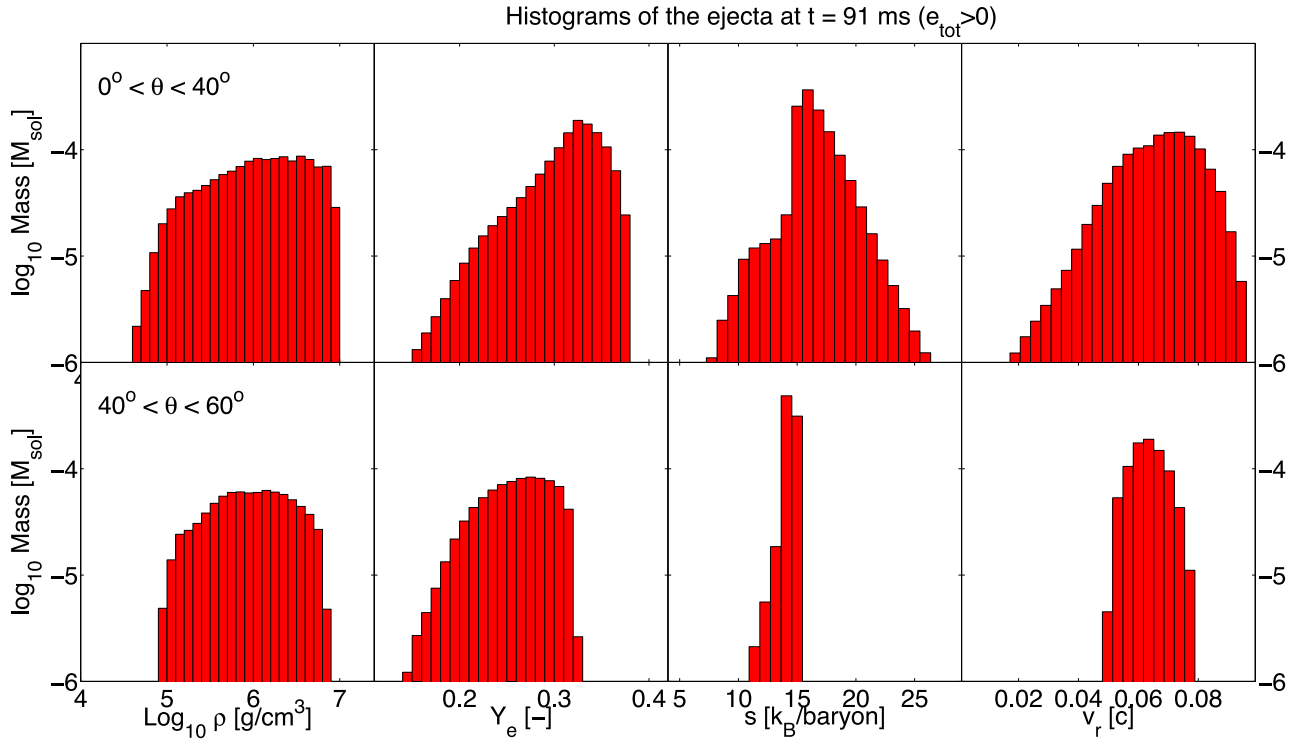

Figure 17. Distributions in the ν-driven wind ejecta binned by different physical properties. The different columns refer to density (ρ, left), electron fraction (Y_e, central left), entropy per baryon (s, central right) and radial velocity (v_r, right). The top (bottom) panels refer to high (low) latitudes.

inside the disc are comparable. There are, however, some differences in the temporal evolution: while we observe almost stationary profiles, decreasing on a time-scale comparable with the expected disc lifetime, their luminosities decrease faster. Also the difference between ν_e and $\bar{\nu}_e$ luminosities decreases, leading to $L_{\nu_e} \approx L_{\bar{\nu}_e}$. Both these differences can depend on the different accretion histories: the usage of the 3D initial data (without performing axisymmetric averages) preserves all the initial local perturbations and favours a substantial $\dot{M}$ inside the disc.

The removal and the deposition of energy, operated by neutrinos, are similar in the two cases. As a result, the subsequent disc and wind dynamics agree well with each other. The amount of ejecta and its electron fraction, on the other hand, show substantial differences: at $t \sim 100$ ms, we observe a larger amount of unbound matter, whose electron fraction has significantly increased.

The evolution of a purely Keplerian disc around a HMNS, under the influence of α-viscosity and neutrino self-irradiation, as a function of the lifetime of the central object, has been more recently investigated by Metzger & Fernández (2014). They employ an axisymmetric HD model, coupled with a grey leakage scheme and a light bulb boundary luminosity for the HMNS. They evolve their system for several seconds to study the development of the neutrino-driven wind and of the viscous ejecta. In the case of a long-lived HMNS ($t_{ns} \gtrsim 100$ ms), our results for the wind are qualitatively similar to their findings: we both distinguish between a polar outflow, characterized by larger electron fractions, entropies and expansion time-scales, and a more neutron-rich equatorial outflow. The polar ejecta, mainly driven by neutrino absorption, represent a meaningful, but small fraction of the initial mass of the disc (a few per cent). Quantitative differences, connected with the different initial conditions and the different neutrino treatment, are however present: their entropies and electron fractions are usually larger, especially at polar latitudes.

The importance of neutrinos in neutron star mergers has been recently addressed also by Wanajo et al. (2014). They have shown that the inclusion of both neutrino emission and absorption can increase the ejecta Y_e to a wide range of values (0.1–0.4), leading to the production of all the r-process nuclides from the dynamical ejecta. However, a direct comparison with our work is difficult since (1) their simulation employs a softer EoS that amplifies general relativistic effects, and (2) their analysis is limited to the dynamical ejecta and the influence of neutrinos on it during the first milliseconds after the merger.

5.2 Nucleosynthesis in neutrino-driven winds

During our simulation, we have computed trajectories of representative tracer particles (Lagrangian particles, passively advected in the fluid during the simulation). The related full nucleosynthesis will be explored in more detail in future work. To get a first idea about the possible nucleosynthetic signatures, we have selected 10 tracers, extrapolated and post-processed with a nuclear network. These tracers are equally distributed between the high- and the low-latitude region (5 + 5). Inside each region, we have picked the particles that represent the most abundant conditions in terms of entropy and electron fraction in the ejecta at $t \approx 90$ ms. Table 2 lists parameters of the selected tracers.

For the nucleosynthesis calculations we employ the WinNet nuclear reaction network (Winteler 2012; Winteler et al. 2012), which represents an update of BasNet network code (Thielemann et al. 2011). The ingredients for the network that we use are the same as described in Korobkin et al. (2012). We have also included the

Table 2. Parameters of representative tracers and corresponding nucleosynthesis: electron fraction Y_e, specific entropy per baryon s, average atomic mass $\langle A \rangle_{final}$ and electric charge $\langle Z \rangle_{final}$ of the resulting nuclei, and the total mass fractions of Lanthanides and Actinides in the resulting nucleosynthetic mix. The latter are important for estimating opacities at the location of the tracers.

Tracer	Y_e	s [k_B baryon^{-1}]	$\langle A \rangle_{final}$	$\langle Z \rangle_{final}$	$X_{La,\,Ac}$
L1	0.213	12.46	118.0	46.2	0.04
L2	0.232	11.84	107.1	42.5	0.009
L3	0.253	12.68	98.0	39.2	7×10^{-5}
L4	0.275	12.73	90.2	36.4	1×10^{-7}
L5	0.315	13.68	81.7	33.0	3×10^{-12}
H1	0.273	13.57	93.0	37.4	8×10^{-7}
H2	0.308	14.69	83.3	33.7	6×10^{-11}
H3	0.338	15.36	79.4	32.1	$<10^{-12}$
H4	0.353	16.40	78.4	31.7	$<10^{-12}$
H5	0.373	18.35	76.8	31.0	$<10^{-12}$

feedback of nuclear heating on the temperature, but we ignore its impact on the density, since previous studies have demonstrated that for the purposes of nucleosynthesis this impact can be neglected (Rosswog et al. 2014a). In this exploratory study, we also do not include neutrino irradiation. Instead we use the final value of electron fraction from the tracer to initialize the network. In this way, we effectively take into account the final neutrino absorptions. Our preliminary experiments show that neutrino irradiation has an effect equivalent to vary Y_e by a few per cent, which is a correction that will be addressed in future work. It is also worth mentioning that the situation is even less simple if one takes into account neutrino flavour oscillations, which may alter the composition of the irradiating fluxes significantly, depending on the densities and distances involved (Malkus, Friedland & McLaughlin 2014).

Fig. 18 shows the resulting nucleosynthetic mass fractions, summed up for different atomic masses, and Table 2 lists the averaged properties of the resulting nuclei. As expected, lower electron fractions lead to an r-process with heavier elements, and for the lowest values of Y_e even the elements up to the third r-process peak ($A \sim 190$) can be synthesized. However, due the high sensitivity to the electron fraction, wind nucleosynthesis cannot be responsible for the observed astrophysical robust pattern of abundances of the main r-process elements. On the other hand, it could successfully contribute to the weak r-process in the range of atomic masses from the first to second peak ($70 \lesssim A \lesssim 110$).

Fig. 18 also illustrates that heavier elements tend to be synthesized at lower latitudes, closer to the equatorial plane. This has important consequences for directional observability of associated electromagnetic transients. Material, contaminated with Lanthanides or Actinides, is expected to have opacities that are orders of magnitudes larger than those of iron group elements. Therefore, the corresponding electromagnetic signal is expected to peak in the infrared. Kasen et al. (2013) estimate that as little as $X_{La,Ac} \gtrsim 0.01$ per cent of these 'opacity polluters' could be enough to raise the opacities by a factor of 100. Table 2 lists also the computed mass fraction of the opacity polluters, which turns out to be negligible for high-latitude tracers, while being quite significant for low-latitude ones. We therefore expect that the signal from the wind outflow will look much redder, dimmer and peak later if the outflow is seen from equatorial rather than polar direction. Additionally, if seen from the low latitudes, the signal from the wind outflow can be further obscured by the dynamical ejecta. Thus, for the on-axis orientation the signal has better prospects of detection, therefore

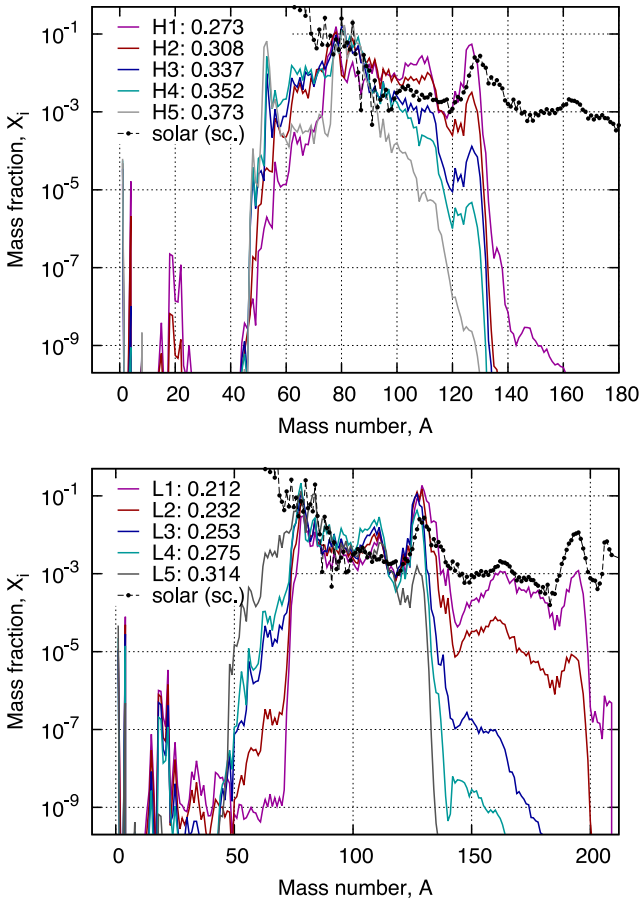

Figure 18. Summed final mass fractions for representative tracers. Top and bottom panels correspond to high-latitude (H1–H5) and low-latitude (L1–L5) tracers, respectively (see Table 2 for parameters of individual tracers). Solar r-process abundances (scaled) are also shown for comparison.

making follow-up observations of short GRBs more promising. We will discuss these questions in detail in Section 5.3 below.

5.3 Electromagnetic transients

In Section 4.4, we have estimated the amount of mass ejected at the end of our simulation ($M_{\rm ej}(t \approx 90\,{\rm ms}) \approx 2.12 \times 10^{-3}\,{\rm M}_\odot$). As discussed there, it needs to be considered as a lower limit on the mass loss at that time. The neutrino emission, however, will continue beyond that time and keep driving the wind outflow. We make here an effort to estimate the total mass loss caused by neutrino-driven winds during the disc lifetime. During our simulation, the temporal evolution of the accretion rate on the HMNS (Fig. 5) is well described by

$$\dot{M}(t) \approx 0.76\,\exp\left[-t/(0.124\,{\rm s})\right]\,{\rm M}_\odot\,{\rm s}^{-1}. \quad (29)$$

We notice that, according to this expression, the total accreted mass is smaller than the initial mass of the disc:

$$M_{\rm acc} \equiv \int_0^\infty \dot{M}\,{\rm d}t \approx 0.095\,{\rm M}_\odot < M_{\rm disc}(t=0) \approx 0.17\,{\rm M}_\odot. \quad (30)$$

This discrepancy can be interpreted as the effect of the wind outflow and of the disc evaporation. The beginning of the latter process has already been observed in our model, but not followed properly due to computational limitations. At $t \approx 0.285$ s the HMNS has accreted 90 per cent of $M_{\rm acc}$. This agrees well with the viscous lifetime of the disc (equation 2), so we consider $t \approx 0.3$ s as a good estimate for the disc lifetime. Since the wind is powered by neutrino absorption, we assume that the mass of the ejecta is proportional to the energy emitted in neutrinos during the disc lifetime:

$$M_{\rm ej}(t = 0.300\,{\rm s}) = \frac{\int_0^{0.300\,{\rm s}} L_{\nu,{\rm cool}}\,{\rm d}t}{\int_0^{0.090\,{\rm s}} L_{\nu,{\rm cool}}\,{\rm d}t}\,M_{\rm ej}(t = 0.090\,{\rm s}). \quad (31)$$

To model $L_\nu(t)$ for $t > 90$ ms, we consider two possible cases:

(A) the HMNS collapses after the disc has been completely accreted;
(B) it collapses promptly at the end of our simulations.

For both cases, we extrapolate linearly the luminosities from Fig. 8. But in case B, we decrease the neutrino luminosity by 50 per cent, to account for the lack of contribution from the HMNS and the innermost part of the disc after the collapse (see Section 4.2). Our final mass extrapolations are listed in Table 3. So in summary, we find 4.87×10^{-3} M$_\odot$ for case A and 3.49×10^{-3} M$_\odot$ for case B. Given that we consider these numbers as lower limits, this implies that the wind would provide a substantial contribution to the total mass lost in a neutron star merger (and likely similar for a neutron star–black hole merger; for an overview over the dynamic ejecta masses see Rosswog et al. 2013).

Table 3. Values of the calculated (top, for $t \approx 90$ ms) and extrapolated (bottom, for $t \approx 300$ ms) ejected masses, for the high (H) and low (L) latitude regions, and their sum. $t_{\rm ns}$ refers to the time-scale for the HMNS to collapse to a black hole.

Case	t (s)	$t_{\rm ns}$ (s)	$M_{\rm ej,H}$ (M$_\odot$)	$M_{\rm ej,L}$ (M$_\odot$)	$M_{\rm ej}$ (M$_\odot$)
A/B	0.09	$\geq$0.09	1.29×10^{-3}	0.82×10^{-3}	2.11×10^{-3}
A	0.3	$>$0.3	2.98×10^{-3}	1.89×10^{-3}	4.87×10^{-3}
B	0.3	$\sim$0.09	2.13×10^{-3}	1.36×10^{-3}	3.49×10^{-3}

With these mass estimates, we compute expected light curves for each tracer, using the semi-analytic spherically symmetric models of macronovae by Kulkarni (2005), the same as the ones described in Grossman et al. (2014). Fig. 19 shows the resulting light curves (top row) for the wind outflow mass from the case A. Each light curve corresponds to a simplified case when the entire wind ejecta evolves according to the thermodynamic conditions of one specific tracer. In this work, we do not take into account spatial or temporal variation of the electron fraction within the wind outflow, but we assume different opacities for the high- and low-latitude tracers. Motivated by recent work of Kasen et al. (2013) and confirmed by Tanaka & Hotokezaka (2013), we take a uniform grey opacity of $\kappa = 10\,{\rm cm}^2\,{\rm g}^{-1}$ for the low-latitude tracers that have a low $Y_{\rm e}$ and produce non-negligible amounts of Lanthanides and Actinides. For the high-latitude, higher $Y_{\rm e}$ tracers we use $1\,{\rm cm}^2\,{\rm g}^{-1}$. The tracers result in a wide variety of potential light curves, whose shape reflects individual nuclear heating conditions for a specific tracer. The middle row of Fig. 19 shows the individual heating rates, normalized to the power law $\dot{\epsilon}_0 = 10^{10} t_{\rm d}^{-1.3}\,{\rm erg\,g^{-1}\,s^{-1}}$. Differences in the shapes of the heating rates for different tracers are due to the dominance of different radioactive elements at late times (Grossman et al. 2014). Despite the variety of macronovae for different tracers, the actual light curve will lie somewhere in between, and the individual differences in the heating rates will be smoothed out. The bottom row represents averaged broad-band light curves from the high- (left-hand panel) and low-latitude (right-hand panel) wind ejecta. The high-latitude case shows a pronounced peak in the B band at

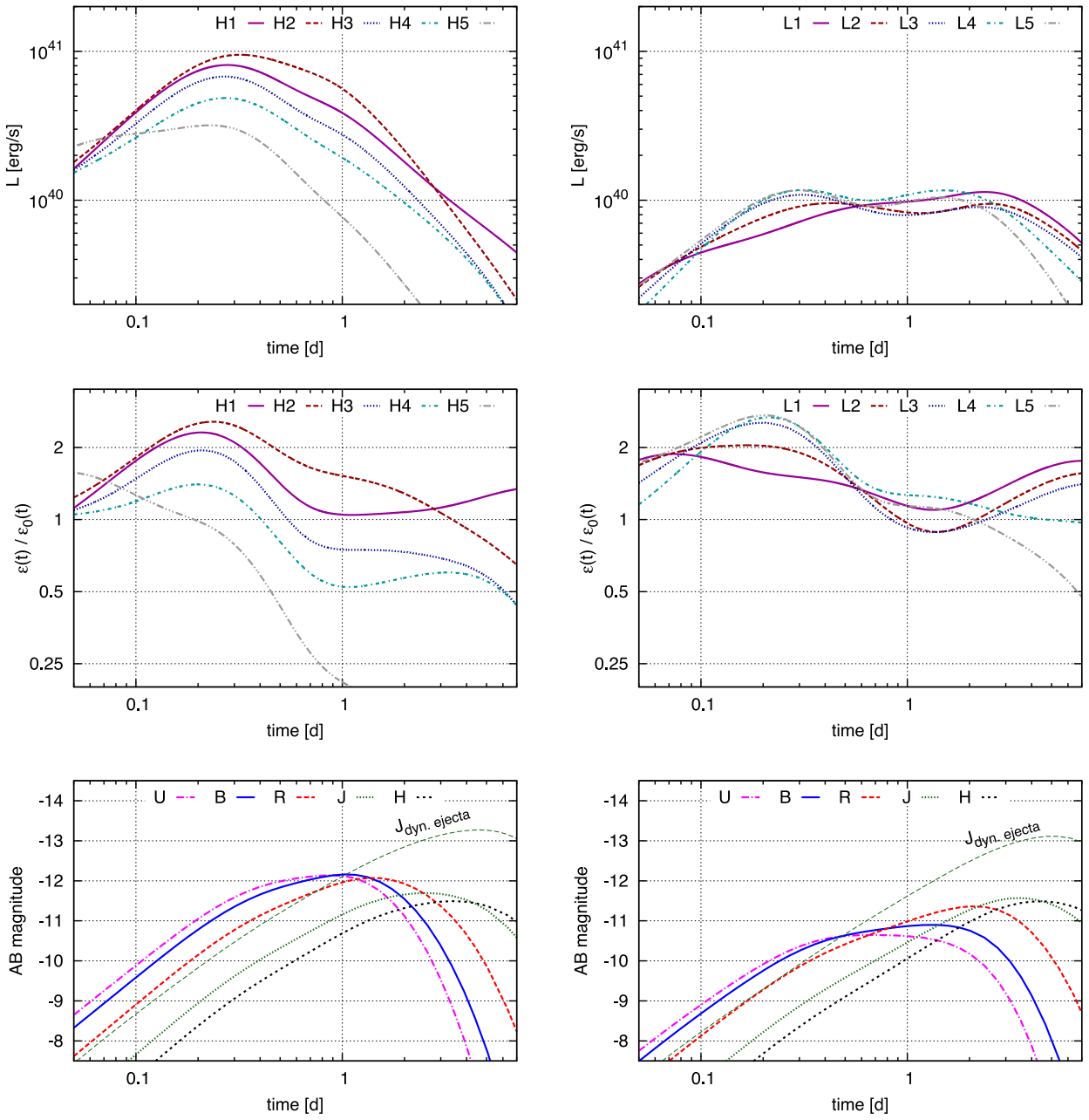

Figure 19. Electromagnetic transients due to the radioactive material produced in the neutrino-driven wind. The left-hand column refers to material ejected at high latitudes (H1-H5), the right-hand column shows the results for the low latitudes (L1–L5). Top row: predicted macronova light curves (bolometric luminosity), calculated with uniform-composition spherically symmetric Kulkarni-type models. Model parameters: ejected mass $m_{\rm ej} = 2 \times 10^{-3}\,{\rm M}_{\odot}$, expansion velocity $v_{\rm e} = 0.08\,c$. Opacity is taken to be 1 and $10\,{\rm cm^2\,g^{-1}}$ for high- and low-latitude tracers, respectively. Middle row: radioactive heating rate for the representative tracers, normalized to $\dot{\epsilon}_0 = 10^{10} t_{\rm d}^{-1.3}$ erg $({\rm g\,s})^{-1}$. Bottom row: broad-band AB magnitudes in five different bands, calculated for the case when the wind outflow is viewed from the 'top' (left-hand panel) and 'side' (right-hand panel). For comparison, the *J*-band signal from the dynamic ejecta is superimposed.

$t \sim 1.3$ d, while the higher opacities for the low-latitude tracers make the light curve dimmer, redder and cause them to peak later.

An interesting question is whether or not the collapse time of the HMNS could possibly be inferred from the EM signal, assuming that the collapse happens after the wind has formed ($t_{\rm ns} \gtrsim 100$ ms). Therefore we compare in Fig. 20 (left-hand panel) the averaged bolometric light curves for the cases A and B of long- and short-lived HMNS. The plot shows the low- and high-latitude components separately, as well as the light curve for the dynamic ejecta for the same merger case. The two cases differ very little, mainly because the mass of the wind component changes only by a factor of ∼1.5, and the light curve is not very sensitive to this mass. The long-lived HMNS (case A) is slightly brighter, but it is not likely that the two cases can be discriminated observationally. The difference between high- and low-latitude regions shows that perhaps geometry of the outflow and its orientation relative to the observer plays much more important role in the brightness and colour of the expected electromagnetic signal. Similarly, there is practically no difference in the

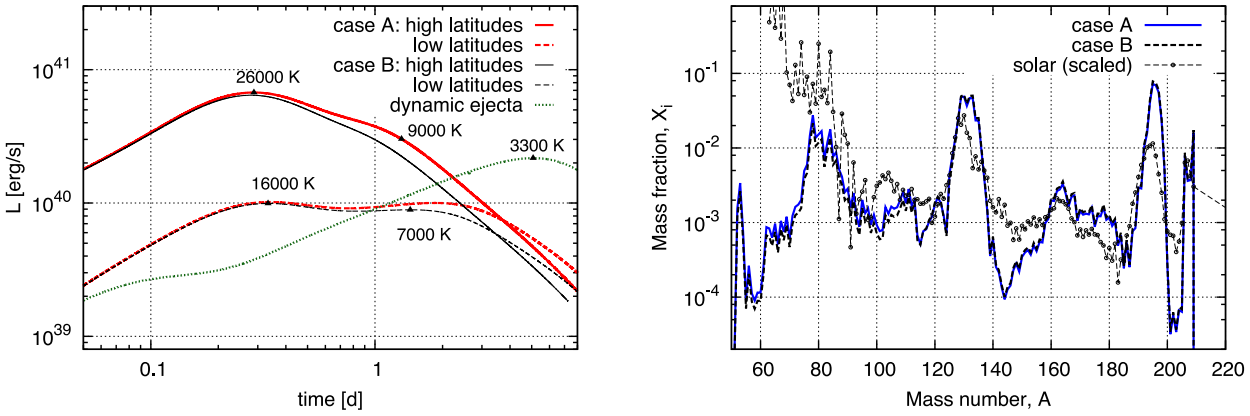

Figure 20. Bolometric light curves (left) and summed abundances (right) for the two cases of a long-lived (case A) and a short-lived (case B) HMNS. The left-hand panel shows separately bolometric light curves of low- and high-latitude outflows, as well as the light curve for the dynamical ejecta from the same merger simulation. The plot also shows the effective temperatures of the macronovae at the key points on the curves. On the right-hand panel, the wind abundances have been added to the abundances from dynamical ejecta, for which we took the total ejected mass of 1.3×10^{-2} $M_\odot$ from the merger simulation.

total summed nucleosynthetic yields for cases A and B (Fig. 20, right-hand panel). Thus it may be difficult to extract the HMNS collapse time-scale from the macronova signal.

6 CONCLUSIONS

We have explored the properties of the neutrino-driven wind that forms in the aftermath of a BNS merger. In particular, we have discussed their implications in terms of the r-process nucleosynthesis and of the electromagnetic counterparts powered by the decay of radioactive elements in the expanding ejecta.

To model the wind, we have performed for the first time 3D Newtonian hydrodynamics simulations, covering an interval of ≈100 ms after the merger, and a radial distance of $\gtrsim$1500 km from the HMNS, with high spatial resolution inside the wind. Neutrino radiation has been treated by a computationally efficient, multiflavour ASL scheme, which includes consistent neutrino absorption rates in optically thin conditions. Our initial configuration is obtained from the direct re-mapping of the matter distribution of a 3D SPH simulation of the merger of two non-spinning 1.4 $M_\odot$ neutron stars (Rosswog & Price 2007, and references therein), at ≈15 ms after the first contact. The consistent dimensionality and the high compatibility between the two models do not require any global average nor any ad hoc assumption for the matter profiles inside the disc.

Our major findings are the following.

(i) The wind provides a substantial contribution to the total mass lost in a BNS merger. At the end of our simulation (≈100 ms after the merger), we compute 2.12×10^{-3} $M_\odot$ of neutron-rich ($0.2 \lesssim Y_e \lesssim 0.4$) ejected matter, corresponding to 1.2 per cent of the initial mass of the disc. We distinguish between a high-latitude (50°–90°) and a low-latitude (30°–50°) component of the ejecta. The former is subject to a more intense neutrino irradiation and is characterized by larger Y_e, entropies and expansion velocities. We estimate that, on the longer disc lifetime, the ejected mass can increase to $3.49–4.87 \times 10^{-3}$ $M_\odot$, where the smaller (larger) value refers to a quick (late) HMNS collapse after the end of our simulation.

(ii) The tendency of Y_e to increase with time above 0.3, especially at high latitudes, suggests a relevant contribution to the nucleosynthesis of the weak r-process elements from the wind, in the range of atomic masses from the first to the second peak. Matter ejected closer to the disc plane retains a lower electron fraction (between 0.2 and 0.3), and produces nuclei from the first to the third peak, without providing a robust r-process pattern.

(iii) The geometry of the outflow and its orientation relative to the observer have an important role for the properties of the electromagnetic transient. According to our results, the high-latitude outflow can power a bluer and brighter light curve, that peaks within 1 d after the merger. Because of the partial contamination of Lanthanides and Actinides, the low-latitude ejecta is expected to have higher opacity and to peak later, with a dimmer and redder light curve.

(iv) Unbalanced pressure gradients and viscosity of numerical origin drive an accretion flow inside the disc. A significant fraction of the neutrino luminosity is provided by this accretion process. This fraction is expected to power a (less intense) baryonic wind also if the HMNS collapses to a black hole before the disc consumption. According to our calculations, the collapse time-scale has a minor impact on the possible observables (electromagnetic counterparts and nucleosynthesis yields), at least if the collapse happens after the wind has formed and weak equilibrium had time to establish inside it. Metzger & Fernández (2014) indicate that more meaningful differences can be potentially seen, in the case of an earlier collapse. This scenario requires further investigations.

Our 3D results show a good qualitative agreement with the 2D results obtained by Dessart et al. (2009) for a similar initial configuration, especially for the neutrino emission and the wind dynamics. Meaningful quantitative differences are still present, probably related to the different accretion and luminosity histories inside the disc. The distinction between a high- and low-latitude region in the ejecta is qualitatively consistent with recent 2D findings of Metzger & Fernández (2014).

The results we have found for the amount of wind ejecta has to be considered as lower limits, since in our model we ignore the effects of magnetic fields and neutrino annihilation in optically thin conditions. In particular, the latter is expected to deposit energy very efficiently in the funnel above the HMNS poles. The calculation of this energy deposition rate for our model and its implication for the sGRB mechanism will be discussed in a future work.

The wind ejecta have to be complemented with the dynamical ejecta and with the outflow coming from the viscous evolution of the disc. These other channels are expected to provide low-latitude

outflows, with an electron fraction similar or lower than the one obtained by the low-latitude wind component (see e.g. Rosswog et al. 2013; Metzger & Fernández 2014, and references therein). Instead, the high-latitude wind component seems to be peculiar in terms of outflow geometry, nucleosynthesis yields and related radioactively powered electromagnetic emission.

This work represents one of the first steps towards a physically consistent and complete model of the aftermath of BNS mergers, including the effect of neutrino irradiation. Our preliminary calculations regarding the nucleosynthesis and the electromagnetic counterparts motivate further analysis and investigations. Moreover, additional work has to be done to develop more accurate and complete radiation hydrodynamics treatments, to include other relevant physical ingredients (like magnetic fields and general relativity), and to explore the present uncertainties in terms of nuclear matter properties and neutrino physics.

ACKNOWLEDGEMENTS

The authors thank M. Hempel for providing the TM1 EoS in tabular form, and F. K. Thielemann for useful discussions and for reading the manuscript. AP and AA were supported by the Helmholtz-University Investigator grant no. VH-NG-825. The work of SR has been supported by the Swedish Research Council (VR) under grant 621-2012-4870. RMC and ML acknowledge the support from the HP2C Supernova project and the ERC grant FISH. AP, SR and ML thank the MICRA-2009 Workshop and the Niels Bohr Institute for their hospitality during the summer of 2009, when this project started. AP thanks the Jacobs University Bremen for its hospitality in 2010 February, 2010 October and 2012 April, and the Stockholm University for its hospitality in 2013 June. SR thanks the University of Basel for its hospitality in 2010 June. AP and SR thank COMPSTAR for the Short Visit Grants 3369 and 3536. AP, RMC, RK and ML thank the use of computational resources provided by the Swiss SuperComputing Center (CSCS), under the allocation grants s414. The SPH simulations for the project have been performed on the facilities of the Höchstleistungsrechenzentrum Nord (HLRN).

REFERENCES

Abbott B. P. et al., 2009, Rep. Progress Phys., 72, 076901
Acernese F. et al., 2008, Classical Quantum Gravity, 25, 114045
Antoniadis J., Freire P. C. C., Wex N., Tauris T. M., Verbiest J. P. W., Whelan D. G., 2013, Science, 340, 448
Arcones A., Janka H.-T., Scheck L., 2007, A&A, 467, 1227
Bacca S., Hally K., Liebendörfer M., Perego A., Pethick C. J., Schwenk A., 2012, ApJ, 758, 34
Barnes J., Kasen D., 2013, ApJ, 775, 18
Bauswein A., Goriely S., Janka H.-T., 2013, ApJ, 773, 78
Beloborodov A. M., 2008, in Axelsson M., ed., AIP Conf. Ser. Vol. 1054, Hyper-accreting Black Holes. Am. Inst. Phys., New York, p. 51
Berger E., 2011, New Astron. Rev., 55, 1
Berger E., 2013, preprint (arXiv e-prints)
Berger E., Fong W., Chornock R., 2013, ApJ, 774, L23
Bruenn S. W., 1985, ApJS, 58, 771
Burrows A., Reddy S., Thompson T. A., 2006, Nucl. Phys. A, 777, 356
Caballero O. L., McLaughlin G. C., Surman R., 2012, ApJ, 745, 170
Davies M. B., Benz W., Piran T., Thielemann F. K., 1994, ApJ, 431, 742
Demorest P. B., Pennucci T., Ransom S. M., Roberts M. S. E., Hessels J. W. T., 2010, Nature, 467, 1081
Dessart L., Ott C. D., Burrows A., Rosswog S., Livne E., 2009, ApJ, 690, 1681
Duncan R. C., Shapiro S. L., Wasserman I., 1986, ApJ, 309, 141
Eichler D., Livio M., Piran T., Schramm D. N., 1989, Nature, 340, 126
Fernández R., Metzger B. D., 2013, MNRAS, 435, 502
Fischer T., Whitehouse S. C., Mezzacappa A., Thielemann F.-K., Liebendörfer M., 2010, A&A, 517, A80
Freiburghaus C., Rosswog S., Thielemann F., 1999, ApJ, 525, L121
Gehrels N., Ramirez-Ruiz E., Fox D. B., 2009, ARA&A, 47, 567
Goodman J., 1986, ApJ, 308, L51
Goriely S., Bauswein A., Janka H.-T., 2011a, ApJ, 738, L32
Goriely S., Chamel N., Janka H.-T., Pearson J. M., 2011b, A&A, 531, A78
Grossman D., Korobkin O., Rosswog S., Piran T., 2014, MNRAS, 439, 757
Hannestad S., Raffelt G., 1998, ApJ, 507, 339
Harry G. M. LIGO Scientific Collaboration, 2010, Classical Quantum Gravity, 27, 084006
Hempel M., Fischer T., Schaffner-Bielich J., Liebendörfer M., 2012, ApJ, 748, 70
Hotokezaka K., Kiuchi K., Kyutoku K., Muranushi T., Sekiguchi Y.-i., Shibata M., Taniguchi K., 2013, Phys. Rev. D, 88, 044026
Hüdepohl L., Müller B., Janka H.-T., Marek A., Raffelt G. G., 2010, Phys. Rev. Lett., 104, 251101
Janka H.-T., 1991, A&A, 244, 378
Käppeli R., Whitehouse S. C., Scheidegger S., Pen U.-L., Liebendörfer M., 2011, ApJS, 195, 20
Kasen D., Badnell N. R., Barnes J., 2013, ApJ, 774, 25
Kiuchi K., Sekiguchi Y., Kyutoku K., Shibata M., 2012, Classical Quantum Gravity, 29, 124003
Korobkin O., Rosswog S., Arcones A., Winteler C., 2012, MNRAS, 426, 1940
Kulkarni S. R., 2005, preprint (arXiv e-prints)
Kyutoku K., Ioka K., Shibata M., 2013, Phys. Rev. D, 88, 041503
Lattimer J. M., Schramm D. N., 1974, ApJ, 192, L145
Lattimer J. M., Schramm D. N., 1976, ApJ, 210, 549
Lattimer J. M., Mackie F., Ravenhall D. G., Schramm D. N., 1977, ApJ, 213, 225
Lee W. H., Ramirez-Ruiz E., 2007, New J. Phys., 9, 17
Lee W. H., Ramirez-Ruiz E., López-Cámara D., 2009, ApJ, 699, L93
Li L.-X., Paczyński B., 1998, ApJ, 507, L59
Liebendörfer M., Rampp M., Janka H., Mezzacappa A., 2005, ApJ, 620, 840
McLaughlin G. C., Surman R., 2005, Nucl. Phys. A, 758, 189
Malkus A., Friedland A., McLaughlin G. C., 2014, preprint (arXiv e-prints)
Melandri A. et al., 2013, GRB Coordinates Network, 14735, 1
Metzger B. D., Fernández R., 2014, MNRAS, 441, 3444
Metzger B. D., Piro A. L., Quataert E., 2008, MNRAS, 390, 781
Metzger B. D., Piro A. L., Quataert E., 2009, MNRAS, 396, 304
Metzger B. D., Arcones A., Quataert E., Martínez-Pinedo G., 2010a, MNRAS, 402, 2771
Metzger B. D. et al., 2010b, MNRAS, 406, 2650
Meyer B. S., 1989, ApJ, 343, 254
Mezzacappa A., Bruenn S. W., 1993, ApJ, 405, 669
Mihalas D., Mihalas B. W., 1984, Foundations of Radiation Hydrodynamics. Oxford Univ. Press, New York
Monaghan J. J., 2005, Rep. Progress Phys., 68, 1703
Mösta P. et al., 2014, ApJ, 785, L29
Murguia-Berthier A., Montes G., Ramirez-Ruiz E., De Colle F., Lee W. H., 2014, ApJ, 788, L8
Nakar E., 2007, Phys. Rep., 442, 166
Narayan R., Paczynski B., Piran T., 1992, ApJ, 395, L83
Neilsen D., Liebling S. L., Anderson M., Lehner L., O'Connor E., Palenzuela C., 2014, Phys. Rev. D, 89, 104029
Oechslin R., Janka H., Marek A., 2007, A&A, 467, 395
Paczynski B., 1986, ApJ, 308, L43
Perego A., Gafton E., Cabezon R., Rosswog S., Liebendoerfer M., 2014, preprint (arXiv e-prints)
Piran T., 2004, Rev. Modern Phys., 76, 1143
Press W. H., Teukolsky S. A., Vetterling W. T., Flannery B. P., 1992, Numerical Recipes in Fortran. The Art of Scientific Computing. Cambridge Univ. Press, New York
Price D. J., 2012, J. Comput. Phys., 231, 759
Price D. J., Rosswog S., 2006, Science, 312, 719

Qian Y.-Z., Woosley S. E., 1996, ApJ, 471, 331
Raffelt G. G., 2001, ApJ, 561, 890
Roberts L. F., Woosley S. E., Hoffman R. D., 2010, ApJ, 722, 954
Roberts L. F., Kasen D., Lee W. H., Ramirez-Ruiz E., 2011, ApJ, 736, L21
Rohlf J. W., 1994, Modern Physics from [alpha] to Z. Wiley, New York
Rosswog S., 2005, ApJ, 634, 1202
Rosswog S., 2009, New Astron. Rev., 53, 78
Rosswog S., 2014a, Living Rev. Comput. Astrophys., submitted
Rosswog S., 2014b, preprint (arXiv e-prints)
Rosswog S., Liebendörfer M., 2003, MNRAS, 342, 673
Rosswog S., Price D., 2007, MNRAS, 379, 915
Rosswog S., Ramirez-Ruiz E., 2002, MNRAS, 336, L7
Rosswog S., Liebendörfer M., Thielemann F.-K., Davies M. B., Benz W., Piran T., 1999, A&A, 341, 499
Rosswog S., Davies M. B., Thielemann F.-K., Piran T., 2000, A&A, 360, 171
Rosswog S., Ramirez-Ruiz E., Davies M. B., 2003, MNRAS, 345, 1077
Rosswog S., Piran T., Nakar E., 2013, MNRAS, 430, 2585
Rosswog S., Korobkin O., Arcones A., Thielemann F.-K., Piran T., 2014, MNRAS, 439, 744
Ruffert M., Janka H.-T., Schaefer G., 1996, A&A, 311, 532
Ruffert M., Janka H., Takahashi K., Schaefer G., 1997, A&A, 319, 122
Sekiguchi Y., Kiuchi K., Kyutoku K., Shibata M., 2011, Phys. Rev. Lett., 107, 051102
Shakura N. I., Sunyaev R. A., 1973, A&A, 24, 337
Shen H., Toki H., Oyamatsu K., Sumiyoshi K., 1998a, Nucl. Phys. A, 637, 435
Shen H., Toki H., Oyamatsu K., Sumiyoshi K., 1998b, Progress Theor. Phys., 100, 1013
Somiya K., 2012, Classical Quantum Gravity, 29, 124007
Springel V., 2010, ARA&A, 48, 391
Surman R., McLaughlin G. C., Hix W. R., 2006, ApJ, 643, 1057
Surman R., McLaughlin G. C., Ruffert M., Janka H.-T., Hix W. R., 2008, ApJ, 679, L117
Symbalisty E. M. D., Schramm D. N., 1982, Astrophys. Lett., 22, 143
Tanaka M., Hotokezaka K., 2013, ApJ, 775, 113
Tanaka M., Hotokezaka K., Kyutoku K., Wanajo S., Kiuchi K., Sekiguchi Y., Shibata M., 2014, ApJ, 780, 31
Tanvir N. R., Levan A. J., Fruchter A. S., Hjorth J., Hounsell R. A., Wiersema K., Tunnicliffe R. L., 2013, Nature, 500, 547
Thielemann F.-K. et al., 2011, Progress Part. Nucl. Phys., 66, 346
Thompson T. A., 2003, ApJ, 585, L33
Timmes F. X., Swesty F. D., 2000, ApJS, 126, 501
Wanajo S., Janka H.-T., 2012, ApJ, 746, 180
Wanajo S., Sekiguchi Y., Nishimura N., Kiuchi K., Kyutoku K., Shibata M., 2014, ApJ, 789, L39
Winteler C., 2012, PhD thesis, Univ. Basel
Winteler C., Käppeli R., Perego A., Arcones A., Vasset N., Nishimura N., Liebendörfer M., Thielemann F.-K., 2012, ApJ, 750, L22

APPENDIX A: THE OPTICAL DEPTH AND THE ASL SCHEME

A1 Optical depth calculation

The values of the spectral optical depths (τ_νs) at each point are calculated using a local ray-by-ray method. It consists of integrating equations (21) and (22) along several predefined paths and taking the minimum values among them. These paths are straight oriented segments, connecting the considered point with the edge of the computational domain. Because of the intrinsically global character of these integrations, we decided to exploit also here the expected symmetry of the remnant, and to calculate τ_ν in axial symmetry. The seven different paths we explore in the ($R_{\rm cyl}$–z) plane are shown in Fig. A1. As a future step, we plan to include the more sophisticated and geometrically more flexible MODA methods (Perego et al. 2014) to compute τ_ν.

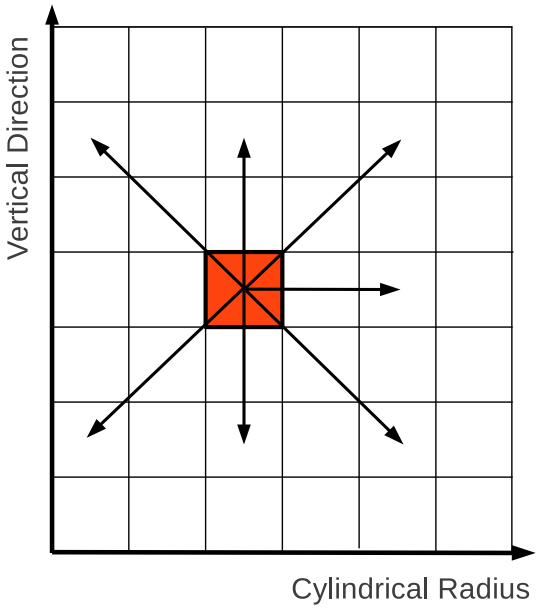

Figure A1. Schematic plot of the seven directions (paths) used to compute the optical depth at each point of the cylindrical domain.

The optical depths vary largely and they decrease, following the density profile, proceeding from the HMNS to the edge of the remnant. To characterize this behaviour, we define the unit vector

$$\hat{\boldsymbol{n}}_\tau \equiv -\nabla\tau_{\nu,\rm sc}/\left|\nabla\tau_{\nu,\rm sc}\right|, \tag{A1}$$

computed at each point of the domain from finite differences on the grid. This vector will be crucial to model the diffusion and the final emission of the neutrinos.

According to the value of $\tau_{\nu,\rm sc}$, we distinguish between three disjoint volumes: (1) $V_{\rm thin}$, for the optically thin region ($\tau_{\nu,\rm sc} \ll 2/3$); (2) $V_{\rm surf}$, for the neutrino surface region[6] ($\tau_{\nu,\rm sc} \sim 2/3$); (3) $V_{\rm thick}$, for the optically thick region ($\tau_{\nu,\,\rm sc} \gg 2/3$). Obviously, $V = V_{\rm thick} \cup V_{\rm surf} \cup V_{\rm thin}$.

A2 The ASL scheme

Since the ASL scheme is spectral, all the terms on the right-hand side of equations (23)–(25) are energy-integrated values of spectral emission (r_ν), absorption (h_ν) and stress ($\boldsymbol{a}_\nu$) rates:

$$R^n_\nu = \int_0^{+\infty} r_\nu\, E^{n+2}\, {\rm d}E, \tag{A2}$$

$$H^n_\nu = \int_0^{+\infty} h_\nu\, E^{n+2}\, {\rm d}E, \tag{A3}$$

$$\left(\frac{{\rm d}\boldsymbol{v}}{{\rm d}t}\right)_\nu = \int_0^{+\infty} \boldsymbol{a}_\nu\, E^2\, {\rm d}E. \tag{A4}$$

The calculation of r_ν, h_ν and $\boldsymbol{a}_\nu$ is the ultimate purpose of the ASL scheme. In Table A1 we have summarized the most important quantities appearing in the scheme, their definitions and relations.

[6] In principle, the neutrino surfaces should have no volume. However, due to the discretization on the (axisymmetric) grid we adopted to calculate τ, every neutrino surface is replaced by a shell of width $\sim\Delta x$. This thin layer is formed by the cells $\boldsymbol{x}$ inside which τ is expected to become equal to 2/3.

Table A1. List of the most important spectral quantities appearing in the ASL scheme (left-hand column) and their definition (central column). In the right-hand column, we list the relevant quantities (spectral quantities and source terms) that depend directly on each table entry. See the text for more details.

Quantity	Definition	Related quantities
$j_{\rm em}$	Emissivity	$r_{\nu,\,\rm prod}$
$k_{\rm ab}$	Absorption opacity	λ_ν, τ_ν, h_ν, $\boldsymbol{a}_\nu$
$k_{\rm sc}$	Scattering opacity	λ_ν, τ_ν
λ_ν	Mean free path	$r_{\nu,\,\rm diff}$
τ_ν	Optical depth	$\hat{\boldsymbol{n}}_\tau$, $\hat{\boldsymbol{n}}_{\rm path}$, $r_{\nu,\,\rm diff}$, $r_{\nu,\,\rm ult}$, h_ν, $\boldsymbol{a}_\nu$
$\hat{\boldsymbol{n}}_\tau$	Opposite τ gradient	$\hat{\boldsymbol{n}}_{\rm path}$, n_ν, $\boldsymbol{s}_\nu$
$\hat{\boldsymbol{n}}_{\rm path}$	Diffusion direction	$r_{\nu,\,\rm ult}$
$r_{\nu,\,\rm prod}$	Production rate	r_ν
$r_{\nu,\,\rm diff}$	Diffusion rate	r_ν
r_ν	Emission rates	$r_{\nu,\,\rm ult}$, $({\rm d}Y_{\rm e}/{\rm d}t)_\nu$, $({\rm d}e/{\rm d}t)_\nu$
$r_{\nu,\,\rm ult}$	Ultimate emission rates	n_ν, $\boldsymbol{s}_\nu$
n_ν	Particle density	h_ν
$\boldsymbol{s}_\nu$	Momentum density	$\boldsymbol{a}_\nu$
h_ν	Absorption rate	$({\rm d}Y_{\rm e}/{\rm d}t)_\nu$, $({\rm d}e/{\rm d}t)_\nu$
$\boldsymbol{a}_\nu$	Stress	$({\rm d}\boldsymbol{v}/{\rm d}t)_\nu$

The spectral emission rates r_ν are calculated as smooth interpolation between diffusion ($r_{\nu,\,\rm diff}$) and production ($r_{\nu,\,\rm prod}$) spectral rates. We compute $r_{\nu,\,\rm prod}$ and $r_{\nu,\,\rm diff}$ as

$$r_{\nu,\rm prod} = \frac{4\pi}{(hc)^3}\frac{j_{\rm em}}{\rho}, \tag{A5}$$

$$r_{\nu,\rm diff} = \frac{4\pi}{(hc)^3}\frac{f_\nu^{\rm FD}}{\rho\, t_{\nu,\rm diff}}, \tag{A6}$$

where $j_{\rm em}$ is the neutrino spectral emissivity, while $f_\nu^{\rm FD}$ is the Fermi-Dirac distribution function for a neutrino gas in thermal and weak equilibrium with matter. $t_{\nu,\,\rm diff}$ is the local diffusion time-scale, calculated as

$$t_{\nu,\rm diff} = \alpha_{\rm diff}\frac{\tau_{\nu,\rm sc}^2\,\lambda_{\nu,\rm sc}}{c}, \tag{A7}$$

where $\lambda_{\nu,\,\rm sc} = (\rho(k_{\nu,\,\rm ab} + k_{\nu,\,\rm sc}))^{-1}$ is the total mean free path. $\alpha_{\rm diff}$ is a constant set to 3. The interpolation formula for r_ν is provided by half of the harmonic mean between the production and diffusion rates.

We compute the spectral heating rate as the properly normalized product of the absorption opacity $k_{\nu,\,\rm ab}$ and of the spectral neutrino density n_ν:

$$h_\nu = c\,k_{\nu,\rm ab}\,n_\nu\,\mathcal{F}_{{\rm e},\nu}\,\mathcal{H}. \tag{A8}$$

$\mathcal{H} \equiv \exp(-\tau_{\nu,\rm sc})$ is an exponential cut-off that ensures the application of the heating term only outside the neutrino surface, and $\mathcal{F}_{{\rm e},\nu}$ is the Pauli blocking factor for electrons or positrons in the final state. n_ν is defined so that the energy-integrated particle density N_ν is given by

$$N_\nu = \int_0^{+\infty} n_\nu\,E^2\,{\rm d}E. \tag{A9}$$

The stress term is calculated similarly to the neutrino heating rate:

$$\boldsymbol{a}_\nu = c\,k_{\nu,\rm ab}\,\boldsymbol{s}_\nu\,\mathcal{F}_{{\rm e},\nu}\,\mathcal{H}, \tag{A10}$$

where $\boldsymbol{s}_\nu$ is the spectral density of linear momentum associated with the streaming neutrinos, while $\mathcal{H}$ and $\mathcal{F}_{{\rm e},\nu}$ are defined as in equation (A8).

In the following, we make use of the volume decomposition ($V = V_{\rm thick} \cup V_{\rm surf} \cup V_{\rm thin}$) and on the definition of $\boldsymbol{n}_\tau$ (equation A1) introduced in Appendix A1 . The quantities n_ν and $\boldsymbol{s}_\nu$ are computed using a multidimensional ray-tracing algorithm. This algorithm assumes that neutrinos (possibly after having diffused from the optically thick region) are *ultimately* emitted isotropically at the neutrino surface and in the optically transparent region. If we define $l_\nu(\boldsymbol{x}', \hat{\boldsymbol{n}})$ as the specific rate per unit solid angle of the radiation emitted from a point $\boldsymbol{x}' \in (V_{\rm surf} \cup V_{\rm thin})$, in the direction $\hat{\boldsymbol{n}}$, then

$$n_\nu(\boldsymbol{x}) = \int_{V_{\rm surf}\cup V_{\rm thin}} \rho\,\frac{l_\nu\left(\boldsymbol{x}', \hat{\boldsymbol{n}}(\boldsymbol{x},\boldsymbol{x}')\right)}{c\,|\boldsymbol{x}' - \boldsymbol{x}|^2}\,{\rm d}^3\boldsymbol{x}' \tag{A11}$$

and

$$\boldsymbol{s}_\nu(\boldsymbol{x}) = \int_{V_{\rm surf}\cup V_{\rm thin}} \rho\,\frac{l_\nu\left(\boldsymbol{x}', \hat{\boldsymbol{n}}(\boldsymbol{x},\boldsymbol{x}')\right)}{c\,|\boldsymbol{x}' - \boldsymbol{x}|^2}\,\frac{E}{c}\,\hat{\boldsymbol{n}}(\boldsymbol{x},\boldsymbol{x}')\,{\rm d}^3\boldsymbol{x}', \tag{A12}$$

where $\hat{\boldsymbol{n}}(\boldsymbol{x},\boldsymbol{x}') = (\boldsymbol{x}' - \boldsymbol{x})/(|\boldsymbol{x}' - \boldsymbol{x}|)$. The isotropic character of the emission allows us to introduce the angle-integrated *ultimate emission rates* $r_{\nu,\,\rm ult}$ as

$$l_\nu(\hat{\boldsymbol{n}}) = \begin{cases} r_{\nu,\rm ult}/\,(2\pi) \text{ if } \hat{\boldsymbol{n}}\cdot\hat{\boldsymbol{n}}_\tau \geq 0, \\ 0 \text{ otherwise.} \end{cases} \tag{A13}$$

$r_{\nu,\,\rm ult}$ and r_ν can differ locally, but they have to provide the same cooling (spectral) luminosities:

$$\int_V \rho\,r_\nu\,{\rm d}V = \int_V \rho\,r_{\nu,\rm ult}\,{\rm d}V. \tag{A14}$$

Since $r_{\nu,\,\rm ult}$ represents the ultimate emission rate, *after* the diffusion process has drained neutrinos from the opaque region to the neutrino surface, $r_{\nu,\,\rm ult} = 0$ inside $V_{\rm thick}$. On the other hand, inside $V_{\rm thin}$ diffusion does not take place and $r_{\nu,\,\rm ult} = r_\nu$. In light of this, equation (A14) becomes

$$\int_{V_{\rm thick}\cup V_{\rm surf}} \rho\,r_\nu\,{\rm d}^3\boldsymbol{x} = \int_{V_{\rm surf}} \rho\,r_{\nu,\rm ult}\,{\rm d}^3\boldsymbol{x}. \tag{A15}$$

Equation (A15) has a clear physical interpretation: inside $V_{\rm surf}$, $r_{\nu,\,\rm ult}$ is obtained (1) from the emission rate, r_ν, at the neutrino surface and (2) from the re-mapping of the emission rates obtained in the opaque region on to the neutrino surface, as a consequence of the diffusion process. A careful answer to this re-mapping problem would rely on the solution of the diffusion equation in the optically thick regime and of the Boltzmann equation in the semi-transparent region. The ASL algorithm calculates the amount of neutrinos diffusing from a certain volume element. But it does not provide information about the angular dependence of their flux, neither about the point of the neutrino surface where they are ultimately emitted. Thus, a phenomenological model is required. When the properties of the system under investigation change on a time-scale larger than (or comparable to) the relevant diffusion time-scale (see Section 2), the neutrino fluxes can be considered as quasi-stationary. Under these conditions, the statistical interpretation of the optical depth, as the average number of interactions experienced by a neutrino before escaping, suggests to consider $\hat{\boldsymbol{n}}_\tau$ as the local preferential direction for neutrino fluxes. While in the (semi-)transparent regime, this unitary vector provides already the favourite emission direction (see equation A13), in the diffusion regime we have to take into account the spatial variation of $\hat{\boldsymbol{n}}_\tau$. To this end, at each point $\boldsymbol{x}$ in

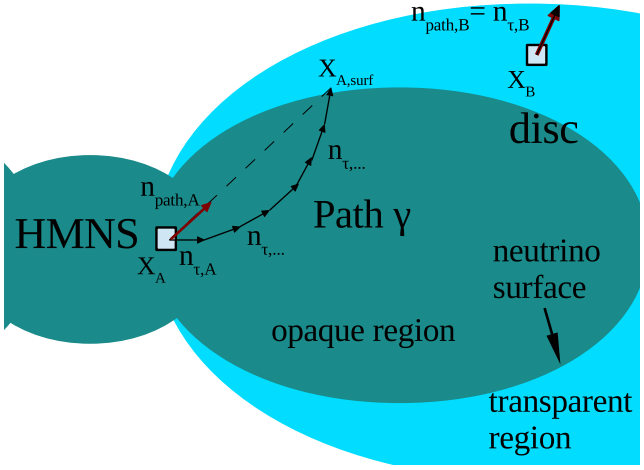

Figure A2. Schematic representation of the procedure to calculate the ultimate emission rates at the neutrino surface and in the optically thin region, $r_{\nu,\,\mathrm{ult}}$, from the emission rates, r_ν. The thin black arrows represent the inverse of the gradient of τ_{sc} ($\hat{\boldsymbol{n}}_\tau$), while the thick red arrow is $\hat{\boldsymbol{n}}_{\mathrm{path}}$. Label x_{A} refers to a point inside the neutrino surface (opaque region), while x_{B} is a point inside the disc, but in the optically thin zone, for which $\hat{\boldsymbol{n}}_{\mathrm{tau}} = \hat{\boldsymbol{n}}_{\mathrm{path}}$. See the text for more details.

V_{thick}, we associate a point $\boldsymbol{x}_{\mathrm{surf}}(\boldsymbol{x})$ in V_{surf} and a related preferential direction

$$\hat{\boldsymbol{n}}_{\mathrm{path}}(\boldsymbol{x}) = \frac{\boldsymbol{x}_{\mathrm{surf}}(\boldsymbol{x}) - \boldsymbol{x}}{|\boldsymbol{x}_{\mathrm{surf}}(\boldsymbol{x}) - \boldsymbol{x}|}, \tag{A16}$$

according to the following prescription: the points $\boldsymbol{x}$ and $\boldsymbol{x}_{\mathrm{surf}}$ are connected by a non-straight path γ that has $\hat{\boldsymbol{n}}_\tau$ as local gradient: $\gamma(s) : [0, 1] \rightarrow [\boldsymbol{x}, \boldsymbol{x}_{\mathrm{surf}}]$, $\boldsymbol{x} \in V_{\mathrm{thick}}$, $\boldsymbol{x}_{\mathrm{surf}} \in V_{\mathrm{surf}}$ and $\mathrm{d}\gamma/\mathrm{d}s = \boldsymbol{n}_\tau$. This procedure is sketched in Fig. A2.

Once $\hat{\boldsymbol{n}}_{\mathrm{path}}$ has been calculated everywhere inside V_{thick}, we can re-distribute the neutrinos coming from the optically thick region on the neutrino surface. This is done assuming that neutrinos coming from a point $\boldsymbol{x}$ are emitted preferentially from points of the neutrino surface located around $\boldsymbol{x}_{\mathrm{surf}}(\boldsymbol{x})$. More specifically, from points $\boldsymbol{x}'$ for which (1) $\boldsymbol{x}' \in V_{\mathrm{surf}}$ and (2) $\mu(\boldsymbol{x}, \boldsymbol{x}') \equiv \hat{\boldsymbol{n}}(\boldsymbol{x}, \boldsymbol{x}') \cdot \hat{\boldsymbol{n}}_{\mathrm{path}}(\boldsymbol{x}) > 0$, where $\hat{\boldsymbol{n}}(\boldsymbol{x}, \boldsymbol{x}') \equiv \left(\boldsymbol{x}' - \boldsymbol{x}\right) / \left|\boldsymbol{x}' - \boldsymbol{x}\right|$. If $\hat{\boldsymbol{n}}$ and $\hat{\boldsymbol{n}}_{\mathrm{path}}$ are close to the parallel condition (i.e. $\mu \approx 1$) we expect more neutrinos than in the case of perpendicular directions (i.e. $\mu \approx 0$). We smoothly model this effect assuming a μ^2 dependence.

The global character of this re-mapping procedure represents a severe computational limitation for our large, 3D, MPI parallelized Cartesian simulation. In order to make the calculation feasible, we take again advantage of the expected high degree of axial symmetry of remnant (especially in the innermost part of it, where the diffusion takes place and most of the neutrino are emitted), and we compute $r_{\nu,\,\mathrm{ult}}$ in axisymmetry.

This paper has been typeset from a TEX/LATEX file prepared by the author.